

## ARTICLE

# Dscam2 suppresses synaptic strength through a PI3K-dependent endosomal pathway

G. Lorenzo Odierna<sup>1</sup>, Sarah K. Kerwin<sup>1</sup>, Lucy E. Harris<sup>1</sup>, Grace Ji-eun Shin<sup>1,3</sup>, Nickolas A. Lavidis<sup>1</sup>, Peter G. Noakes<sup>1,2</sup>, and S. Sean Millard<sup>1</sup>

**Dscam2 is a cell surface protein required for neuronal development in *Drosophila*; it can promote neural wiring through homophilic recognition that leads to either adhesion or repulsion between neurites. Here, we report that *Dscam2* also plays a post-developmental role in suppressing synaptic strength. This function is dependent on one of two distinct extracellular isoforms of the protein and is autonomous to motor neurons. We link the PI3K enhancer, *Centaurin gamma 1A*, to the *Dscam2*-dependent regulation of synaptic strength and show that changes in phosphoinositide levels correlate with changes in endosomal compartments that have previously been associated with synaptic strength. Using transmission electron microscopy, we find an increase in synaptic vesicles at *Dscam2* mutant active zones, providing a rationale for the increase in synaptic strength. Our study provides the first evidence that *Dscam2* can regulate synaptic physiology and highlights how diverse roles of alternative protein isoforms can contribute to unique aspects of brain development and function.**

## Introduction

Cell recognition molecules are key players in the development of the nervous system. Some regulate connections between neurons by promoting axon guidance, target selection, and boundary formation, whereas others critically regulate synaptic physiology, growth, and maintenance (Shapiro et al., 2007). The number of cell recognition molecules encoded by the human genome is small (Almén et al., 2009) compared with the trillions of connections in the brain. Several different mechanisms could account for these numerical differences including combinatorial interactions (Thu et al., 2014), alternative splicing (Nilsen and Graveley, 2010), and the ability of these proteins to perform multiple functions (Neuhaus-Follini and Bashaw, 2015).

*Dscam2* has been primarily studied in the *Drosophila* visual system, where it functions as a tiling receptor and is required for both postsynaptic specificity and dendritic targeting of lamina neurons (Millard et al., 2007; Millard et al., 2010; Tadros et al., 2016). Alternative splicing of *Dscam2* produces two distinct extracellular protein isoforms, *Dscam2A* and *Dscam2B*. These proteins differ at a single immunoglobulin domain, and this domain confers biochemical specificity for homophilic recognition (Millard et al., 2007). Alternative splicing of *Dscam2* is cell type specific; most neurons analyzed thus far express either *Dscam2A* or *Dscam2B*, but not both (Lah et al., 2014; Tadros et al., 2016). This cell type specificity is driven in part by the splicing factor *Muscleblind*, which represses the selection of *Dscam2*

exon 10A and is necessary for the selection of exon 10B (Li and Millard, 2019). Because homophilic binding does not occur between different isoforms (Millard et al., 2010; Özkan et al., 2013), only neurons that express the same isoform can induce signaling downstream of homophilic interactions. Thus, cell-specific expression of *Dscam2* isoforms could be analogous to having two different genes that perform similar functions in different cells. One prediction of this model is that expression of a single isoform in all *Dscam2*-positive cells should generate the same gain-of-function phenotypes with either isoform. Indeed, this is what was previously observed in visual system neurons (Lah et al., 2014; Kerwin et al., 2018; Tadros et al., 2016).

In addition to regulating connectivity between neurons, cell recognition molecules can also modulate synaptic processes (Thalhammer and Cingolani, 2014). For example, *FasII* was originally discovered as an axon guidance molecule required for fasciculation (Grenningloh et al., 1991; Lin et al., 1994) but was later shown to play a role in synaptic plasticity (Stewart et al., 1996; Schuster et al., 1996). The ability of neurons to modulate neurotransmitter release within a dynamic range is critical for processes that require synaptic potentiation and depression (Yang and Calakos, 2013), such as learning (Lynch, 2004). If a synapse were to function at maximal capacity, an increase in synaptic strength (potentiation) would not be possible. Thus, intracellular signaling pathways that inhibit neurotransmitter

<sup>1</sup>School of Biomedical Sciences, The University of Queensland, Brisbane, Australia; <sup>2</sup>Queensland Brain Institute, The University of Queensland, Brisbane, Australia; <sup>3</sup>Mortimer B. Zuckerman Mind Brain Behavior Institute, Columbia University, New York, NY.

Correspondence to S. Sean Millard: [s.millard@uq.edu.au](mailto:s.millard@uq.edu.au).

© 2020 Odierna et al. This article is distributed under the terms of an Attribution–Noncommercial–Share Alike–No Mirror Sites license for the first six months after the publication date (see <http://www.rupress.org/terms/>). After six months it is available under a Creative Commons License (Attribution–Noncommercial–Share Alike 4.0 International license, as described at <https://creativecommons.org/licenses/by-nc-sa/4.0/>).

release function as “brakes” that permit further synaptic potentiation (Cooper and Bear, 2012), and cell surface receptors that regulate these pathways form a line of communication between neurons and their extracellular environment. Several studies have demonstrated that endosomes play a central role in this process by integrating intracellular signals that modulate neurotransmitter release (Hauswirth et al., 2018). Rab5, for example, is required to maintain early endosome identity and morphology but has been found to also act as a rate-limiting molecule for presynaptic neurotransmitter release (Wuchterpfennig et al., 2003). High levels of Rab5 at synapses are associated with increased release, and impairment of Rab5 causes a decrease in neurotransmitter output (Wuchterpfennig et al., 2003). Further, loss of the Rab35 GTPase-activating protein, Skywalker, results in increased neurotransmitter release and aberrant endosomal morphology (Uytterhoeven et al., 2011). Although we are beginning to understand the downstream intracellular processes that enact changes to synaptic strength in order to maintain neuronal plasticity (Delvendahl and Müller, 2019; Frank, 2014), much less is known about the upstream cell recognition molecules that regulate their activity.

Previous studies indicate that *Dscam2* predominantly functions to regulate neuronal connectivity during development. Whether it can influence the physiology of synapses after they form is currently not known. In this study, we discovered that *Dscam2* is expressed in motor neurons of *Drosophila* larvae and exploited this well-characterized system to ask whether *Dscam2* influences various aspects of synaptic physiology. When we stimulated motor neurons and recorded postsynaptic muscle responses, we found that *Dscam2* mutant synapses were stronger than controls. Interestingly, this effect of suppressing synaptic strength was also observed when motor neurons expressed the incorrect isoform of *Dscam2* (*Dscam2A*). We identified the PI3K enhancer, Centaurin Gamma 1A (CenG1A), as a component of the *Dscam2*-mediated synaptic pathway and found changes in specific phosphoinositides and endosomal compartments in the *Dscam2* mutants that were previously implicated in regulating synaptic strength (Uytterhoeven et al., 2011; Fernandes et al., 2014; Wuchterpfennig et al., 2003). To understand how these changes in endosomal compartments led to increased neurotransmitter release, we used electron microscopy to analyze synaptic vesicle distribution at active zones and found an increase in the *Dscam2* mutants. Our results indicate that *Dscam2* regulates a phosphatidylinositol-3 kinase (PI3K)-dependent endosomal pathway that suppresses the deposition of synaptic vesicles at active zones, providing a compelling example of how an alternative isoform of a developmental molecule can be temporally reemployed for unique purposes in the nervous system.

## Results

### *Dscam2B* but not *Dscam2A* is expressed in the peripheral nervous system (PNS)

Using previously described isoform-specific transcriptional reporter lines (Lah et al., 2014), we first characterized *Dscam2* isoform expression within the larval ventral nerve cord (VNC)

and peripheral nervous system (PNS). *Dscam2A* expression was restricted to the VNC, whereas *Dscam2B* was expressed in the VNC and in neurons that project through peripheral nerves (Fig. 1, A and B'). This was confirmed by co-labeling neuromuscular junctions (NMJs) with the neuronal membrane marker anti-HRP and the *Dscam2A* reporter (Fig. 1, C–C'). By contrast, *Dscam2B* was expressed in the VNC (Fig. 1 B'), motor neurons (Fig. S1 A), and peripheral body-wall sensory neurons (Fig. S1 A'). *Dscam2B* was detectable in ~50% of motor neurons (Table S1), including the type Ib motor neuron that contacts muscles 6 and 7, known as MN6/7-Ib (Fig. 1, D and D'). Interestingly, *Dscam2B* was not detectable in the type Is motor neuron that also connects to these muscles, known as MNSNb/d-Is (Fig. 1, D–D').

To determine whether *Dscam2* functions in the development of the VNC and peripheral neurons, we analyzed *Dscam2* isoform expression throughout embryonic development. Most motor neurons pass major developmental milestones between 12 and 16 h after egg laying (AEL), including responsiveness to the major excitatory neurotransmitter acetylcholine and maturation of currents that underlie action potential firing (Broadie and Bate, 1993; Baines and Bate, 1998). *Dscam2B* was detectable in two small groups of segmentally repeating peripheral and central neurons beginning at 12–16 h AEL (Fig. S1, G–J'), but both isoforms were much more broadly expressed beginning at larval hatching 8 h later (Fig. S1, B–F'). This was interesting, given that by this stage all motor neurons have undergone dendritogenesis and have formed functional synaptic connections with their target muscles (Landgraf et al., 1997). Thus, detectable expression of *Dscam2* does not largely coincide with any major developmental milestone in motor neurons other than hatching. This makes it unlikely that *Dscam2* plays a critical role in the development of motor neuron synapses.

### Increased spontaneous release in *Dscam2* single isoform lines

*Dscam2* regulates specificity at photoreceptor synapses in collaboration with *Dscam1* (Millard et al., 2010), and cell-specific regulation of its extracellular isoforms is necessary for attaining appropriate axon terminal size in lamina neurons (Lah et al., 2014). Whether *Dscam2* is directly required for synaptic maintenance or function, however, has not been investigated. We therefore performed intracellular electrophysiological recordings at the NMJ (Fig. 1 E), where both synaptic morphology and physiology have been well characterized (Menon et al., 2013). To investigate a role for *Dscam2* in synaptic physiology and whether the two different isoforms function equally in this process, we assessed three different *Dscam2* genotypes: null animals (*Dscam2<sup>null</sup>*) and two different transgenic lines of flies that express a single isoform from the endogenous *Dscam2* locus (*Dscam2A* and *Dscam2B*; a full description of single isoform knock-in lines appears in Lah et al. (2014)). This allowed us to determine whether any changes to neuronal physiology were identical in the two single isoform lines, as would be expected if the isoforms function similarly in different cells, and to distinguish between loss- and gain-of-function effects by comparing them with *Dscam2<sup>null</sup>* animals.

To record spontaneous (miniature) excitatory junctional potentials (mEJPs), we used sharp electrodes to impale muscle 6

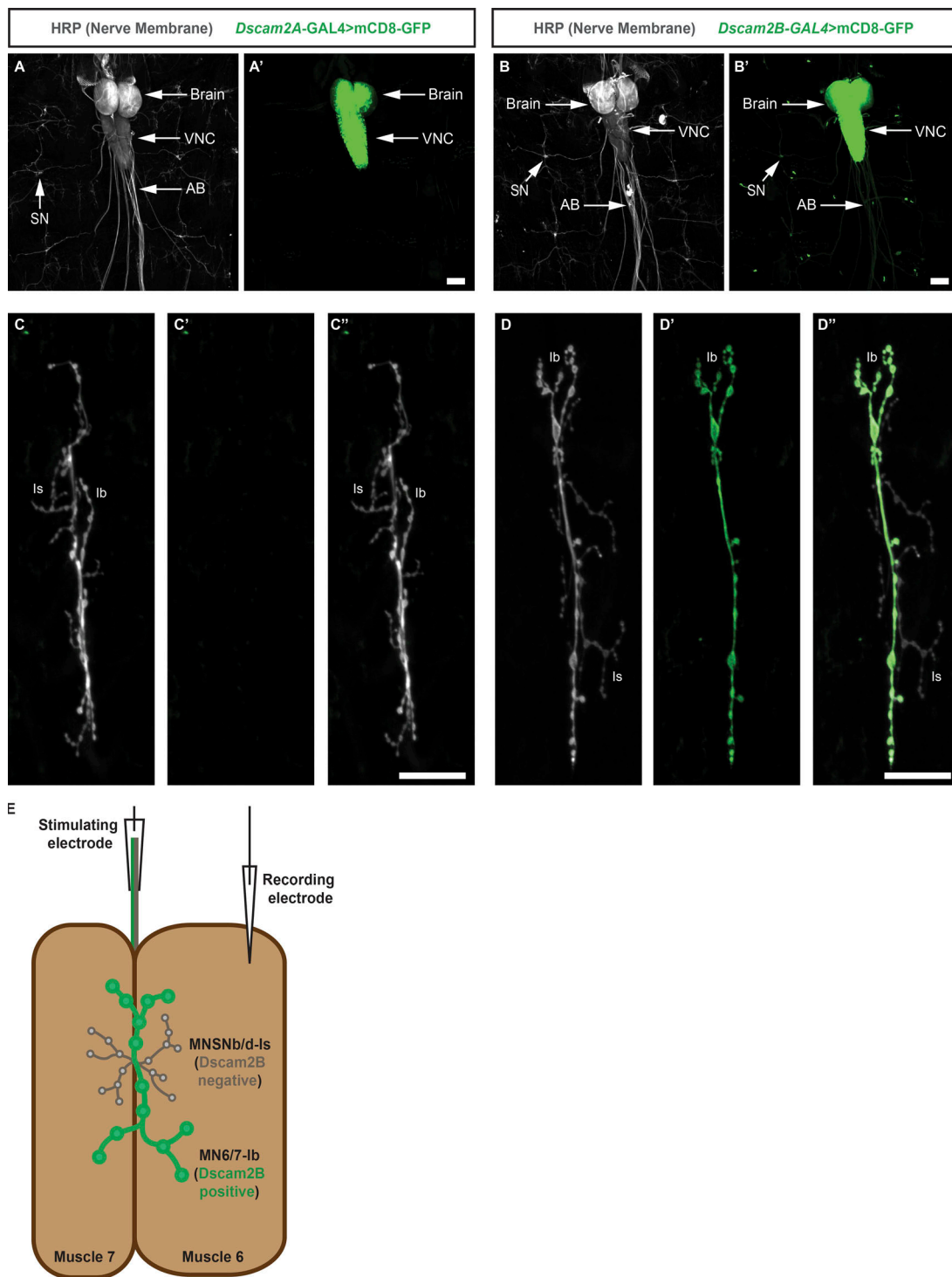


Figure 1. ***Dscam2B*, but not *Dscam2A*, is expressed in the PNS. (A and A')** Co-labeling of HRP (gray) and *Dscam2A*>CD8GFP (green) in filleted larvae shows broad expression of *Dscam2A* in the central nervous system (AB, axon bundle; SN, sensory neuron) and lack of expression in the periphery. Scale bar, 150  $\mu$ m. **(B and B')** Co-labeling of HRP (gray) and *Dscam2B*>CD8GFP (green) in filleted larvae shows broad expression in the central nervous system and PNS. Sensory neurons (SN) can be identified in the body wall as well as axon bundles (AB), which contain afferent motor neuron axons and efferent SN axons. Scale bar, 150  $\mu$ m. **(C–C'')** Co-labeling of HRP (gray) and *Dscam2A*>CD8GFP (green) at motor neuron axon terminals contacting muscles 6/7 confirm lack of *Dscam2A* expression in both Ib and Is. Scale bar, 30  $\mu$ m. **(D–D'')** Co-labeling of HRP (gray) and *Dscam2B*>CD8GFP (green) at motor neuron axon terminals contacting muscles 6/7 confirms that motor neurons express *Dscam2B*. At this NMJ, *Dscam2B* is detectable in Ib and not in Is. Scale bar, 30  $\mu$ m. **(E)** Schematic of electrophysiology setup used in this study. Spontaneous and evoked potentials are recorded from a sharp electrode in muscle 6. The axon bundle innervating muscle 6/7 is stimulated with a second electrode. Two motor neurons innervate these muscles: Ib expresses *Dscam2B*, Is does not.

(Fig. 1 E). Control and *Dscam2<sup>null</sup>* animals exhibited similar mEJP frequencies, whereas the mEJP frequency was dramatically increased in *Dscam2A* and *Dscam2B* (Fig. 2, A and C). We also observed an increase in the mEJP amplitude in both *Dscam2A* and *Dscam2B* single isoform animals, but not *Dscam2<sup>null</sup>*, relative to controls (Fig. 2, B and C). These observations suggest that *Dscam2* is not required to regulate spontaneous neurotransmitter release per se. Instead, removing cell-specific *Dscam2* isoform expression causes a gain-of-function phenotype that promotes spontaneous neurotransmitter release. This effect is likely caused by inappropriate *Dscam2* interactions between neurites within the VNC, such as motor neuron dendrites and interneuron axons, which normally express different isoforms.

### **Dscam2 suppresses synaptic strength**

To test whether *Dscam2* plays a role in regulating evoked neurotransmission, we stimulated motor neurons while recording postsynaptic excitatory junctional potentials (EJPs) in muscle. To investigate different properties of neurotransmission, we tested a range of extracellular calcium concentrations ( $[Ca^{2+}]_o$ ; 0.5, 0.75, 1.5, and 3 mM). If *Dscam2* were to influence action potential propagation or impair exocytic machinery, then changes in the amplitude of evoked potentials would be expected at higher, saturating levels of  $[Ca^{2+}]_o$ , whereas if it were to directly affect neurotransmitter release, effects would be most apparent at lower ranges of  $[Ca^{2+}]_o$  (del Castillo and Katz, 1954a; Jan and Jan, 1976). We did not observe any significant effects at high  $[Ca^{2+}]_o$  (1.5 and 3 mM) for the *Dscam2<sup>null</sup>* and single isoform lines, suggesting that *Dscam2* does not regulate action potential propagation or exocytic machinery in motor neurons (Fig. S2 A). Conversely, strong effects were observed at low  $[Ca^{2+}]_o$  (0.5 mM), suggesting that *Dscam2* influences calcium-dependent aspects of neurotransmitter release. At this concentration of  $[Ca^{2+}]_o$ , used in all following experiments, unless otherwise stated, the EJPs, corrected for nonlinear summation (EJP') in *Dscam2<sup>null</sup>* animals, were increased by 50% compared with controls (Fig. 2, D and E), demonstrating that *Dscam2* normally weakens the evoked synaptic response. Further, *Dscam2A* animals displayed a 74% increase in EJP' amplitude, whereas *Dscam2B* animals had responses that were not significantly different from controls (Fig. 2, D and E). We found that muscle resting membrane potential, EJP width at half maximum, and rise time were not different between any of the genotypes (Fig. S2, D, E, and F, respectively), highlighting the specificity of *Dscam2* for neurotransmitter release. Furthermore, since *Dscam2A* single isoform animals exhibited a loss-of-function phenotype and motor neurons normally express *Dscam2B*, this result suggested that *Dscam2B* is required to suppress synaptic strength.

We next calculated the number of synaptic vesicles released in response to a single presynaptic depolarization (quantal content) by dividing the mean amplitude of the EJPs by the mean amplitude of the mEJPs for each genotype. For the *Dscam2* single isoform mutants, we used the median of mEJP amplitudes because they displayed skewed amplitude frequency distributions (Fig. S2 C). Quantal content was higher in both *Dscam2<sup>null</sup>* and *Dscam2A* animals relative to control and was unchanged in *Dscam2B* animals (Fig. 2 F). Variance-amplitude plots indicated

that this change was predominantly driven by an increase in the probability of neurotransmitter release (Fig. S2 B). These data demonstrate that *Dscam2* normally acts to restrict synaptic strength at the NMJ by suppressing the number of vesicles released in response to an action potential and that *Dscam2B*, the isoform normally expressed in motor neurons, but not *Dscam2A* is able to carry out this function.

To validate the synaptic effects observed in *Dscam2* mutant animals, we used a paired pulse assay, which measures the extent to which evoked release is influenced by changes in release probability and presynaptic calcium-dependent priming (del Castillo and Katz, 1954b; Dudel and Kuffler, 1961). We found that across all measured interstimulus time intervals (20, 50, and 200 ms) the paired-pulse ratio (PPR) was not significantly different between control and *Dscam2B* animals; however, at 20 ms and 50 ms, it was significantly reduced in both *Dscam2<sup>null</sup>* and *Dscam2A* animals (Fig. 2 G). Previous studies have shown that weak synapses tend to facilitate when exposed to paired stimuli, whereas strong synapses do not (Kurdyak et al., 1994). Thus, the PPR results suggest that loss of *Dscam2* results in stronger synapses and provide further evidence that *Dscam2B* can perform a function in motor neurons that *Dscam2A* cannot.

To explore the extent to which the *Dscam2* loss-of-function synaptic effect was autonomous to motor neurons, we knocked down *Dscam2* using upstream activating sequence (UAS) RNAi driven by different GAL4s and measured mEJP, EJP', and quantal content. We found that both pan-neuronal and motor neuron-specific knockdown of *Dscam2* phenocopied the null phenotype, whereas knockdown in muscle (*BG487-GAL4*) had no effect (Fig. 2, H–J). These data highlight the specificity for the requirement of *Dscam2* in regulating synaptic strength and suggest that this requirement is autonomous to motor neurons.

### **Dscam2 mutants exhibit minor changes in NMJ morphology and synaptic markers**

NMJ structure is a strong determinant of synaptic strength. One possible explanation for the neurotransmission defects observed in *Dscam2* mutants is that *Dscam2* might regulate growth of the NMJ, which in turn produces downstream changes in synaptic strength. If this is the case, the increased EJP' and quantal content effects in *Dscam2<sup>null</sup>* larvae may be a result of larger NMJs. However, anti-HRP revealed a small but significant reduction in the total number of boutons per NMJ in *Dscam2<sup>null</sup>*, *Dscam2A*, and *Dscam2B* animals relative to control (Fig. 3, A–E). Muscle size, measured using phalloidin, was also modestly reduced in the single isoform lines, but not in *Dscam2<sup>null</sup>* larvae (Fig. 3 E'). Given that there were fewer boutons in *Dscam2<sup>null</sup>* and *Dscam2A* animals, these data argue against *Dscam2* regulating synaptic strength via NMJ morphology.

We next assessed a panel of synaptic markers in the *Dscam2* mutant lines, including the scaffolding protein brp, which marks active zones (Fig. 3, K–N), the synaptic vesicle protein Synaptotagmin 1 (Syt1; Fig. S3, F–I), and postsynaptic proteins discs-large (dlg; Fig. S3, A–D) and glutamate receptor subunit IIA (GluRIIA; Fig. 3, P–S). None of these markers were different in *Dscam2<sup>null</sup>* larvae compared with controls, failing to provide any structural or molecular correlates for the increased synaptic

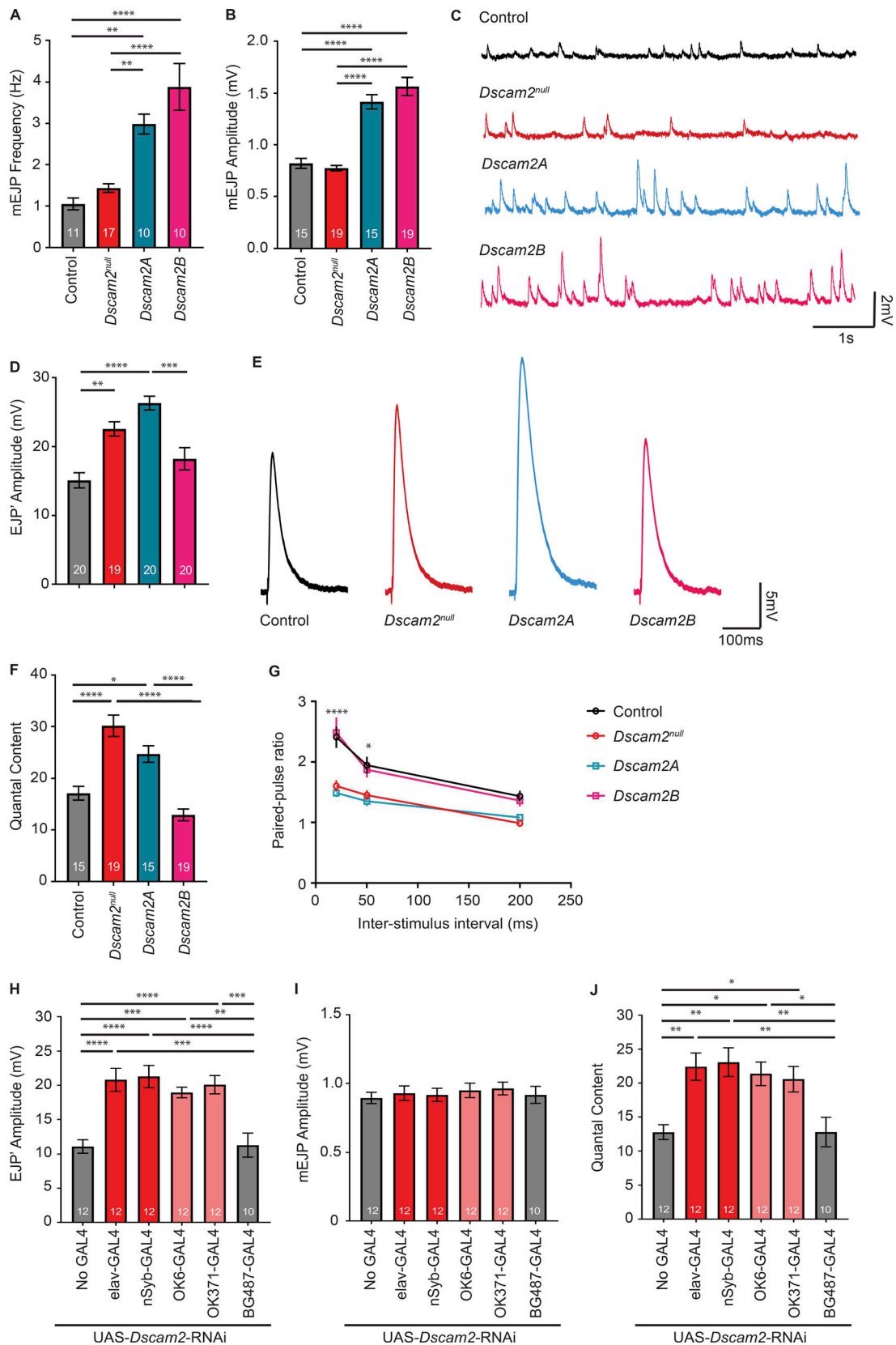


Figure 2. Neurotransmission defects at *Dscam2* mutant NMJs. (A and B) Quantification of mEJP frequency (A) and amplitude (B) in NMJ preparations from control (black), *Dscam2<sup>null</sup>* (red), *Dscam2A* (blue), and *Dscam2B* (magenta; one-way ANOVA, all groups compared with Tukey's post-test). (C) Representative traces of intracellular mEJP recordings. (D) Quantification of the amplitude of evoked potentials (EJP; one-way ANOVA; all groups compared with Tukey's post-test). (E) Representative traces of evoked EJP recordings. (F) Quantification of quantal content, the number of synaptic vesicles released following an evoked

EJP', which is calculated by dividing evoked EJP' by single quanta (mEJP; one-way ANOVA; all groups compared with Tukey's post-test). **(G)** Quantification of PPR across 20-ms, 50-ms, and 200-ms interstimulus intervals ( $n = 9-10$ ; two-way ANOVA; groups within interstimulus interval compared with Tukey's post-test). **(H-J)** Knockdown of *Dscam2* in neurons and muscle. Quantification of EJP' amplitude (H), mEJP amplitude (I), and quantal content (J). UAS-*Dscam2*-RNAi was driven by no Gal4 (control) or the following Gal4 lines: *elav* (all neurons), *nSyb* (all neurons), *OK6* (motor neurons), *OK371* (MNs), and *BG487* (muscle; one-way ANOVA; groups compared with Tukey's post-test). Data shown as mean  $\pm$  SEM;  $n$  indicated in graph. \*,  $P < 0.05$ ; \*\*,  $P < 0.01$ ; \*\*\*,  $P < 0.001$ ; \*\*\*\*,  $P < 0.0001$  for all panels.

strength in these animals (Fig. 3, J, O, and T; and Fig. S3, E and J). Conversely, effects were observed in the single isoform lines, commonly at a similar magnitude for both, including increased bouton size (Fig. 3 J), increased number of brp-positive puncta per bouton (Fig. 3 O), and increased diameter of dlG immunoreactivity surrounding boutons (Fig. S3 E). An increase in the number of active zones per bouton in *Dscam2A* and *Dscam2B* is a significant synaptic change given that it increases the number of sites at which neurotransmitter release can occur. This potentially explains why we detected an increase in mEJP frequency in the single isoform lines. These effects were not observed in the type IIs motor neurons that also contact muscles 6/7, but do not express *Dscam2* (Fig. 3 J', O', T'; and Fig. S3, E' and J'), suggesting that the gain-of-function effects are autonomous to *Dscam2*-expressing neurons.

#### **Dscam2 suppresses synaptic strength via a PI3K-dependent pathway**

To gain insight into the signaling pathways through which *Dscam2* suppresses synaptic strength, we searched the literature for mutations that result in altered evoked neurotransmitter release without affecting spontaneous release or NMJ morphology. The resultant list was short, given how few genes have been found to suppress synaptic strength in *Drosophila*. We then performed a reverse genetic screen by crossing these mutations into a *Dscam2* mutant background and assessing spontaneous and evoked release at the NMJ. Of the eight genes we tested, we identified *Centaurin Gamma 1A* (*CenG1A*), a PI3K enhancer with a GTPase-activating domain (Homma et al., 2014), as a candidate (Fig. S3 K). *CenG1A* has homology to vertebrate PIKs, which play numerous roles in regulating cell signaling by enhancing PI3Ks, binding to membrane receptors, and suppressing apoptotic pathways (Chan and Ye, 2012). A loss-of-function allele of *Drosophila CenG1A* (Gross et al., 2015) was previously shown to increase EJP amplitude and quantal content at the larval NMJ (Homma et al., 2014). We confirmed these results and found that the magnitude of the EJP' increase was very similar between *CenG1A* and *Dscam2* single mutants (Fig. 4, A-C).

We next tested heterozygotes (*Dscam2<sup>null/+</sup>* and *CenG1A<sup>EY01217/+</sup>*) and surprisingly found that EJP' amplitude was consistently elevated in each heterozygote mutant alone. This made it difficult to determine whether the genes were in the same pathway using double-heterozygote combinations because the difference between hetero- and homozygotes was small; therefore, additive and synergistic effects would be expected to be the same. Indeed, double-heterozygotes exhibited an increase in EJP' amplitude and quantal content that was similar to that of either mutant alone and significantly different from that

of controls (Fig. 4, A-C). Consistent with a genetic interaction between these two genes, however, double mutants for *Dscam2* and *CenG1A* were not different from either single homozygous mutant alone (Fig. 4, A-C). This argued against two parallel pathways that independently regulate synaptic strength, as additive effects would have resulted in an EJP' increase that was 2 $\times$  higher than the single mutants alone. Thus, our genetic results suggest that *Dscam2* and *CenG1A* may act within the same pathway to suppress synaptic strength.

One possible model for the interaction between *Dscam2* and *CenG1A* is that *CenG1A* expression, localization, or activity is regulated by *Dscam2*. Given that *CenG1A* is a PI3K enhancer, loss of this gene is expected to affect the levels of phosphoinositides associated with PI3K activity (Gross et al., 2015). In particular, PI(4,5)P<sub>2</sub> (PIP<sub>2</sub>) is a substrate for PI3K, so a decrease in PI3K activity should result in its accumulation. We therefore investigated PIP<sub>2</sub> levels at control and *Dscam2<sup>null</sup>* NMJs by driving expression of a well-characterized PIP<sub>2</sub> reporter (*UAS-PLC $\delta$ PH-mCherry*) in motor neurons (Verstreken et al., 2009). Quantification of PLC $\delta$ PH-mCherry immunofluorescence intensity revealed a dramatic enrichment (threefold increase in MN6/7-Ib terminals) of PIP<sub>2</sub> at *Dscam2<sup>null</sup>* boutons relative to controls (Fig. 4, D-F), providing evidence that *Dscam2* promotes PI3K activity, likely through *CenG1A*, at motor neuron axon terminals. Indeed, PIP<sub>2</sub> levels were also increased at *CenG1A* mutant terminals (Fig. 4, G-I'). Interestingly, the increase in PIP<sub>2</sub> in *Dscam2<sup>null</sup>* animals was observed to a lesser extent in Is boutons (Fig. 4 I'), suggesting that this effect is nonautonomous to *Dscam2*-expressing cells.

Although an increase in PIP<sub>2</sub> can be interpreted as evidence for reduced PI3K activity, it might conversely be the result of increased activity of proteins involved in PIP<sub>2</sub> synthesis, such as PI4P5K (Ishihara et al., 1996). To more directly test the involvement of PI3K, we recorded EJP' amplitude in control and *Dscam2<sup>null</sup>* animals in the presence of two different PI3K inhibitors, Wortmannin and LY294002. The effects of PI3K suppression on neurotransmitter release have been well characterized and demonstrate different outcomes depending on whether PI3K is acutely or chronically inhibited. For example, acute suppression of PI3K using drugs typically results in reduced neurotransmitter release (Cousin et al., 2003; Thyagarajan et al., 2014), whereas chronic suppression using transgenic approaches has the opposite effect, resulting in increased neurotransmitter release (Howlett et al., 2008). Our results with *Dscam2* are consistent with a chronic inhibition of PI3K, resulting in an increase in synaptic release. We reasoned that chronic inhibition of PI3K in *Dscam2<sup>null</sup>* mutants would make these animals less sensitive to PI3K inhibitors. We found

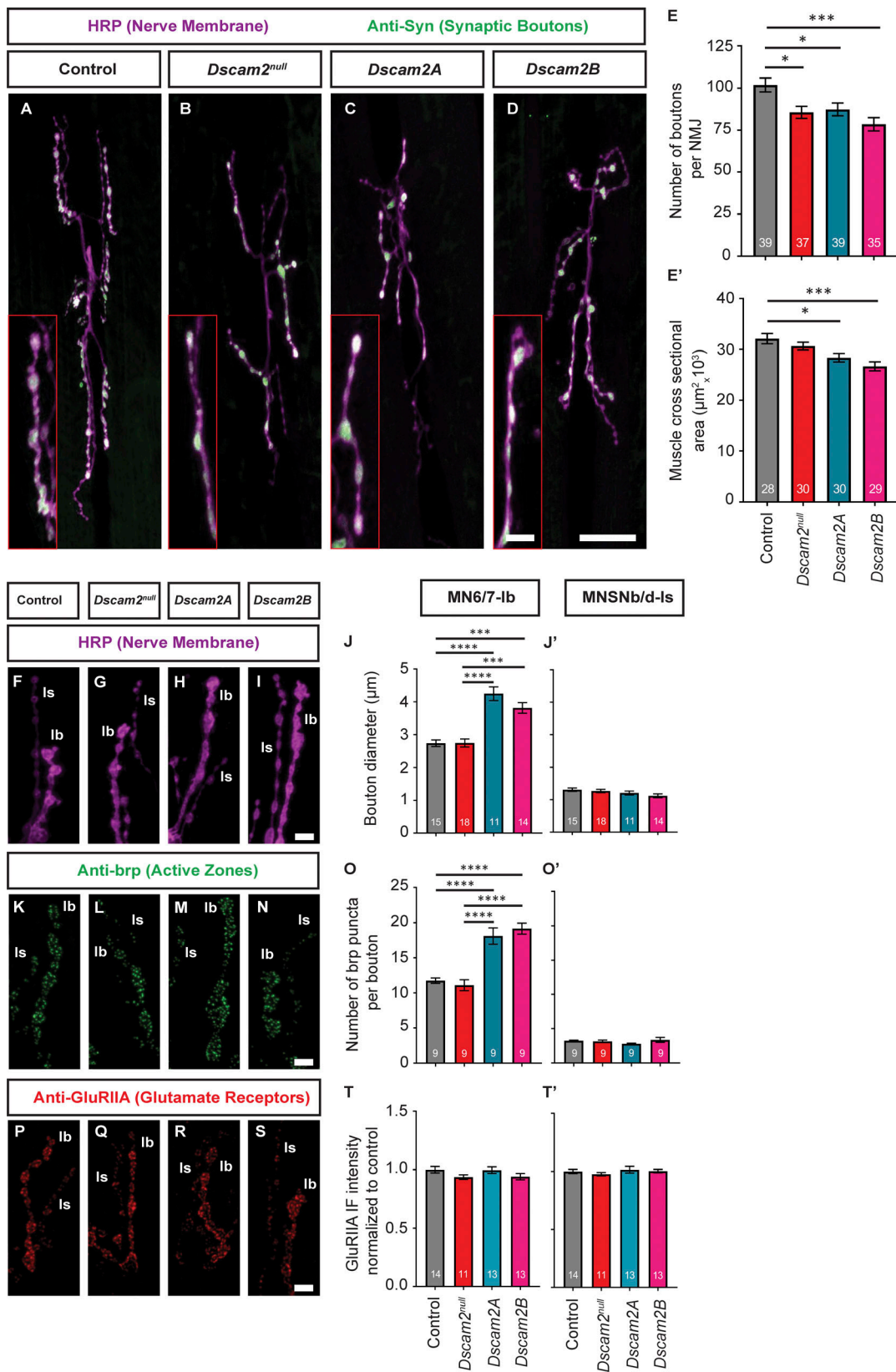


Figure 3. **Morphological phenotypes at the NMJ of *Dscam2* mutants.** (A–D) Representative images of HRP immunoreactivity (magenta) labeling nerve terminal membrane and anti-Syn (green) labeling synaptic boutons in control (A), *Dscam2<sup>null</sup>* (B), *Dscam2A* (C), and *Dscam2B* (D). Scale bar, 20  $\mu\text{m}$ . Inset scale bar, 5  $\mu\text{m}$ . (E and E') Quantification of the absolute number of boutons per NMJ (E) and muscle 6 cross-sectional area (E'). (F–I) Representative images of HRP immunoreactivity (magenta, F–I), which was used to quantify bouton size in Ib (J) and Is (J') axon terminals. Scale bar, 5  $\mu\text{m}$ . (K–O) Representative images of anti-brp immunoreactivity (green, K–N) and quantification of the number of puncta/bouton in Ib (O) and Is (O') boutons. Scale bar, 5  $\mu\text{m}$ . (P–T) Representative

images of GluRIIA immunoreactivity (red, P-S) and quantification of immunofluorescence (IF) intensity normalized to control at Ib (T) and Is (T') boutons. Scale bar, 5  $\mu$ m. Data shown as mean  $\pm$  SEM; *n* indicated in graph; and one-way ANOVA, groups compared with Tukey's post-test. \*,  $P < 0.05$ ; \*\*\*,  $P < 0.001$ ; \*\*\*\*,  $P < 0.0001$  for all panels. IF, immunofluorescence.

that in controls increasing concentrations of both Wortmannin and LY294002 caused a reduction in EJP' amplitude, consistent with previous studies (Cousin et al., 2003; Thyagarajan et al., 2014). In *Dscam2<sup>null</sup>* mutants, however, this decrease was not observed, even at concentrations of LY294002 that produced an  $\sim 60\%$  drop in EJP' amplitude in controls (Fig. 4, J and K). Thus, loss of *Dscam2* results in a robust synaptic resistance to PI3K inhibitors, strongly implicating PI3K in the *Dscam2* pathway for regulation of synaptic strength.

#### Depletion of endosomal markers in *Dscam2* mutants

Endosomal dynamics have been intimately linked to phosphoinositide levels (Jones and Clague, 1995; Tan et al., 2015) and synaptic strength (Uytterhoeven et al., 2011; Fernandes et al., 2014). We therefore next explored whether the increase in synaptic strength in the *Dscam2* mutants could be linked to changes in the synaptic endosome system. Early endosomes contain phosphatidylinositol (PI) phosphorylated at position 3, PI(3)P, on their membranes, and this lipid plays a critical role in recruiting components of the endosome fusion machinery (Wucherpennig et al., 2003). PI(3)P is produced when PI3K phosphorylates PI on endosome membranes (Gillooly et al., 2003). To visualize PI(3)P in *Dscam2<sup>null</sup>* animals, we expressed a well-characterized marker consisting of tandem FYVE domains fused to GFP (2xFYVE-GFP) that bind specifically to PI(3)P (Wucherpennig et al., 2003). Quantification of 2xFYVE-GFP immunofluorescence intensity in *Dscam2<sup>null</sup>* boutons revealed a significant decrease compared to control (Fig. 5, A-E'). The penetrance of this phenotype was variable, with some boutons exhibiting undetectable labeling whereas others were labeled quite well, and the average decrease was  $\sim 30\%$  (Fig. 5, E and E'). Together, these experiments demonstrated that loss of *Dscam2* causes depletion of PI(3)P at motor neuron axon terminals.

After exocytosis, one pathway for membrane recovery is through an endocytic process that produces preendosomal intermediates, which then fuse with endosomes. Synaptic vesicle proteins are sorted at these stations, and new vesicles form and are added to the releasable pool in the nerve terminal (Wucherpennig et al., 2003; Watanabe and Boucrot, 2017). Early endosome accumulation is therefore dependent on (1) the amount of traffic from the early endosome to synaptic vesicle pool, (2) endocytic processes that generate preendosomal intermediates, and (3) activity of protein complexes that promote fusion between these intermediates and the endosome (Gorvel et al., 1991; Wucherpennig et al., 2003; Helenius et al., 1983). We reasoned that if the decrease in 2xFYVE-GFP immunofluorescence intensity in *Dscam2<sup>null</sup>* mutants was due to increased traffic from endosomes to the synaptic vesicle pool, then stimulating exocytosis should result in a further decrease due to increased demand for generation of synaptic vesicles. To test this, we measured 2xFYVE-GFP immunofluorescence intensity

following a KCl-mediated stimulation paradigm to promote robust exocytosis. Interestingly, following stimulation with KCl, 2xFYVE-GFP immunofluorescence intensity was no longer different between control and *Dscam2<sup>null</sup>* animals (Fig. 5, E and E'). This suggested that the decrease must be explained by defects in either endocytosis or in fusion of preendosomal intermediates (Wucherpennig et al., 2003; Watanabe et al., 2013a, 2013b). To distinguish between these two options, we performed a KCl-mediated FM4-64 styryl dye uptake assay, which is a reliable method for investigating gross defects in endocytosis (Verstreken et al., 2008). Following 1 min of stimulation and dye uptake, we found that the average immunofluorescence intensity of FM4-64 in axon terminals was not different between *Dscam2<sup>null</sup>* and control animals (Fig. 5, F-H'). This strongly suggested that the decreased 2xFYVE-GFP signal could not be explained by defective endocytosis, leaving defective fusion between preendosomal intermediates and maturation to PI(3)P-positive endosomes as the most likely explanation for the decreased 2xFYVE-GFP in *Dscam2<sup>null</sup>* mutants.

#### Accumulation of preendosomal intermediates in *Dscam2* mutants

To determine if there were ultrastructural correlates to the endosomal effects that we had observed at the level of light microscopy, we turned to electron microscopy (Fig. 6, A and B). We analyzed synaptic vesicles, dense-core vesicles (DCVs; Fig. 6 C), and several structures attributed to endosomal trafficking including irregularly shaped/tubular endosomes (Fig. 6 D), multivesicular bodies (MVBs; Fig. 6 E), and large (70–80-nm diameter) vesicles (Fig. 6 F). These large vesicles have been shown by others to represent preendosomal intermediates (Wucherpennig et al., 2003; Watanabe et al., 2013a, 2013b). The density of MVBs was unaffected (Fig. 6 G), suggesting late-stage endosomal maturation is not under the control of *Dscam2*. Conversely, *Dscam2<sup>null</sup>* boutons displayed a significant increase in the density of both large vesicles and irregularly shaped/tubular endosomes compared with control boutons (Fig. 6, A, B, H, and I). The near-twofold increase in large vesicle density in *Dscam2<sup>null</sup>* mutants is consistent with a model wherein *Dscam2* promotes fusion of preendosomal intermediates by controlling the level of PI(3)P on their membranes. PI(3)P is necessary for recruiting critical components of the fusion machinery, such as Rab5 (Gillooly et al., 2003). Interestingly, we also found an approximately threefold increase in the density of DCVs in *Dscam2<sup>null</sup>* boutons compared with controls (Fig. 6 J). Given that exocytosis of DCVs is dependent on PI(3)P (Meunier et al., 2005), this finding is consistent with *Dscam2* and CenG1A promoting the activity of PI3Ks at synapses. Interestingly, we also found increased density of DCVs in *Dscam2A* and not in *Dscam2B* single isoform larvae (Fig. S4 F), providing additional evidence for this model.

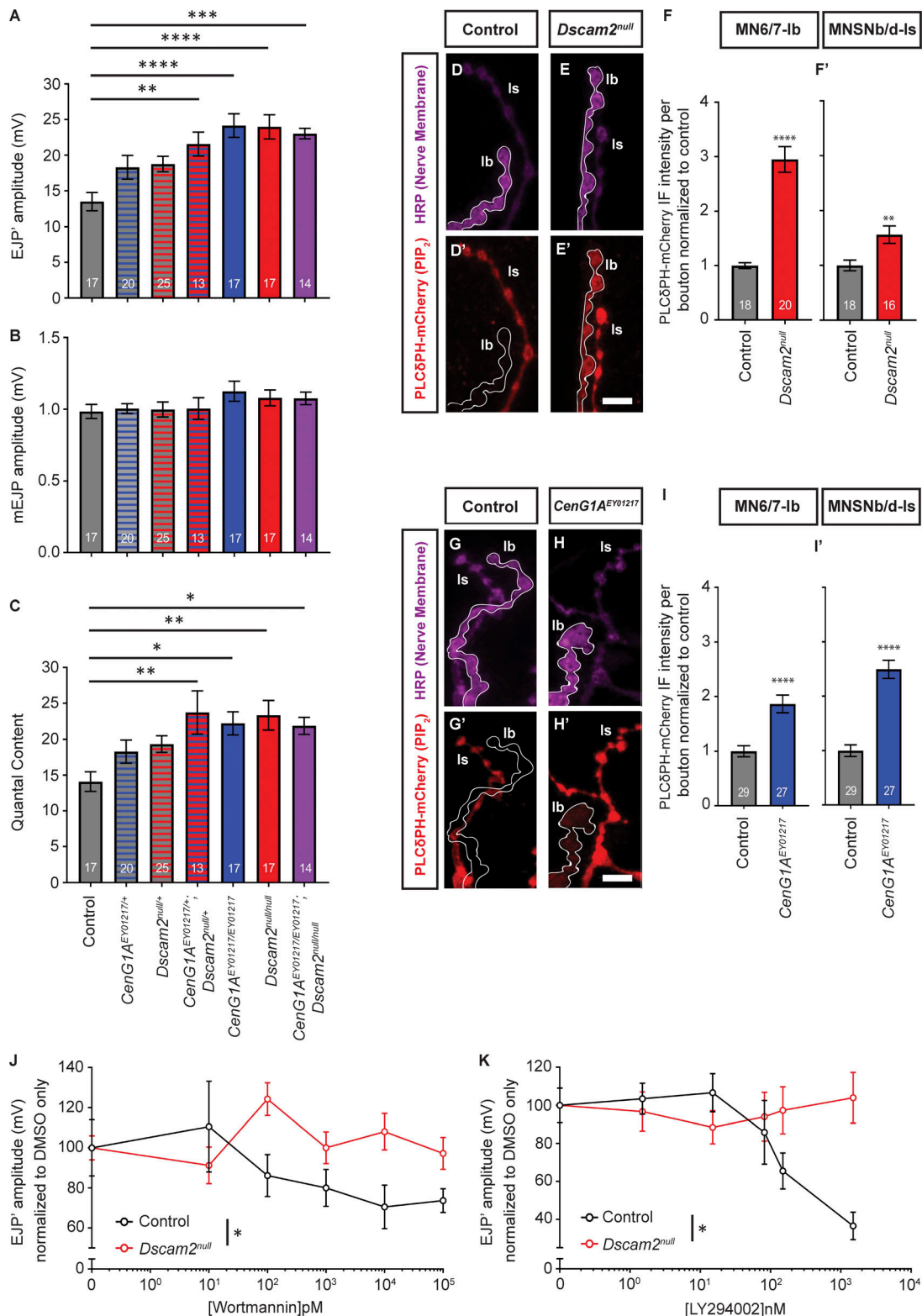


Figure 4. ***Dscam2<sup>null</sup>* mutants exhibit PI3K-deficient phenotypes.** (A–C) Genetic interactions between *Dscam2* and the PI3K enhancer *Centaurin Gamma 1A* (*CenG1A*). Quantification of corrected evoked (A) and spontaneous (B) potential amplitude as well as quantal content (C) for control, *CenG1A<sup>EY01217/+</sup>*, *Dscam2<sup>null/+</sup>*, *CenG1A<sup>EY01217/+</sup>; Dscam2<sup>null/+</sup>*, *CenG1A<sup>EY01217/EY01217</sup>; Dscam2<sup>null/null</sup>*, and *CenG1A<sup>EY01217/EY01217</sup>; Dscam2<sup>null/null</sup>* (EJP' and quantal content analyzed with one-way ANOVA, groups compared with Tukey's post-test; mEJP analyzed with Kruskal-Wallis test, groups compared with Dunn's post-test). (D–E) Representative images of HRP immunoreactivity (magenta, D and E) and anti-mCherry (red, D' and E') from the PIP<sub>2</sub> reporter (PLCδPH-mCherry) in control (*OK6-GAL4/+*; *UAS-PLCδPH-mCherry/+*) and *Dscam2<sup>null</sup>* (*OK6-GAL4/+*; *Dscam2<sup>null</sup>*, *UAS-PLCδPH-mCherry/Dscam2<sup>null</sup>*). Scale bar, 5 μm. (F and F') Quantification of PLCδPH-mCherry immunofluorescence intensity per bouton normalized to control in Ib (F) and Is (F'; unpaired Student's *t* test). (G–H') Representative images of HRP immunoreactivity (magenta, G and H) and anti-mCherry (red, G' and H') from the PIP<sub>2</sub> reporter (PLCδPH-mCherry) in control (*OK6-GAL4/+*;

*UAS-PLCδPH-mCherry/+*) and *CenG1A<sup>EY01217</sup>* (*CenG1A<sup>EY01217</sup>, OK6-GAL4/CenG1A<sup>EY01217</sup>; UAS-PLCδPH-mCherry/+*). Scale bar, 5 μm. **(I and I')** Quantification of PLCδPH-mCherry immunofluorescence. Intensity per bouton normalized to control in Ib (I) and Is (I'; Mann-Whitney rank-sum test). **(J and K)** Quantification of EJP' in control (black) and *Dscam2<sup>null</sup>* (red) in the presence of a titration of the PI3K-inhibiting drugs Wortmannin (J; n = 7–13) and LY294002 (K; n = 9–15); two-way ANOVA omnibus reveals significant differences overall between control and *Dscam2<sup>null</sup>* after application of Wortmannin and LY294002. Data shown as mean ± SEM; n indicated in graph. \*, P < 0.05; \*\*, P < 0.01; \*\*\*, P < 0.001; \*\*\*\*, P < 0.0001 for all panels. IF, immunofluorescence.

**Increased numbers of synaptic vesicles at T-bars of *Dscam2* mutants**

Although we were able to link loss of *Dscam2* to changes in endosomes at the NMJ, we had yet to understand how this relationship affected neurotransmission. To investigate this aspect

at the level of synaptic ultrastructure, we analyzed the density and size of synaptic vesicles in boutons and the number of synaptic vesicles clustered around active zones, which are marked by electron-dense T-bar structures in flies (*Meinertzhagen and O'Neil, 1991*). We found that synaptic

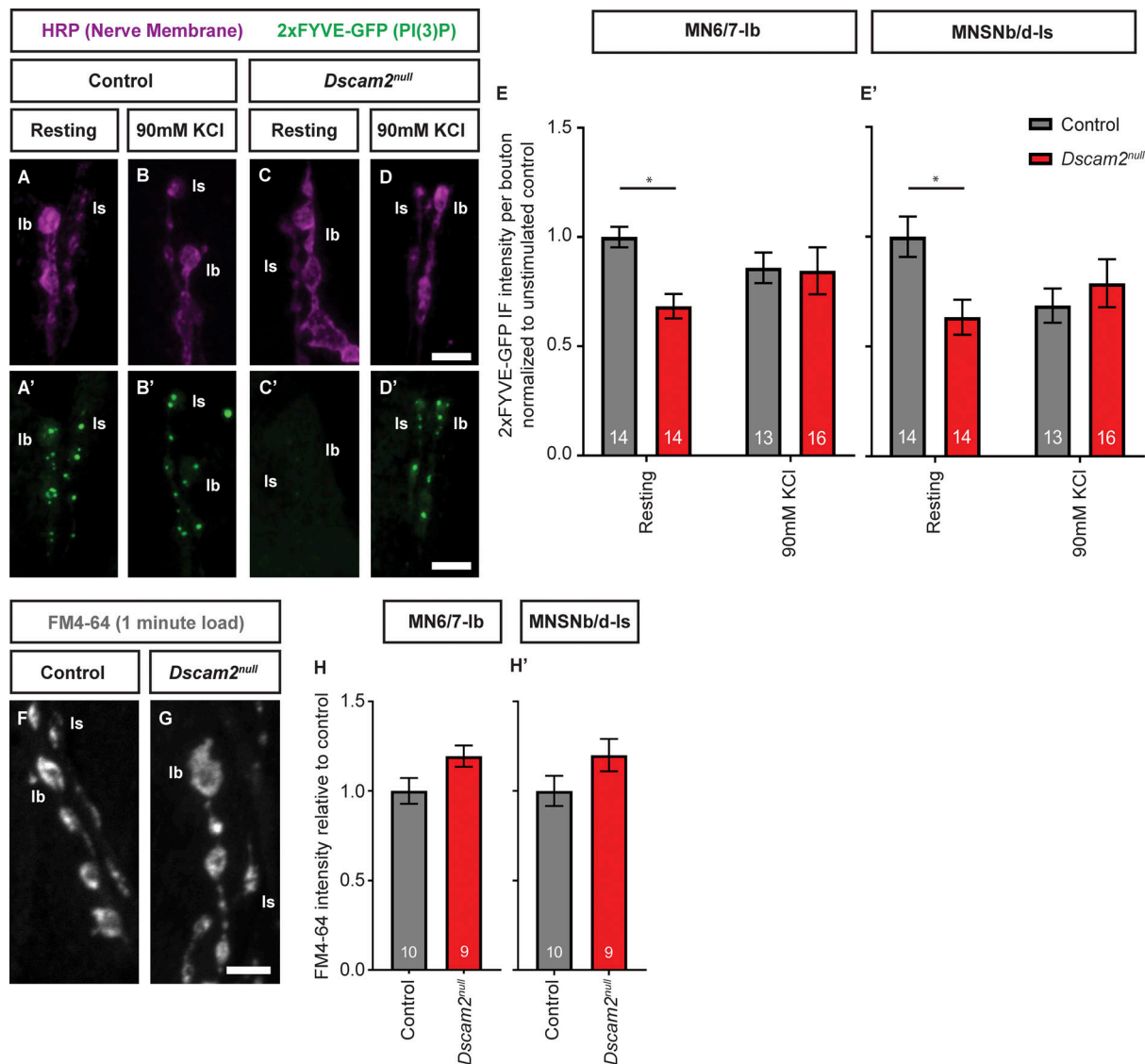
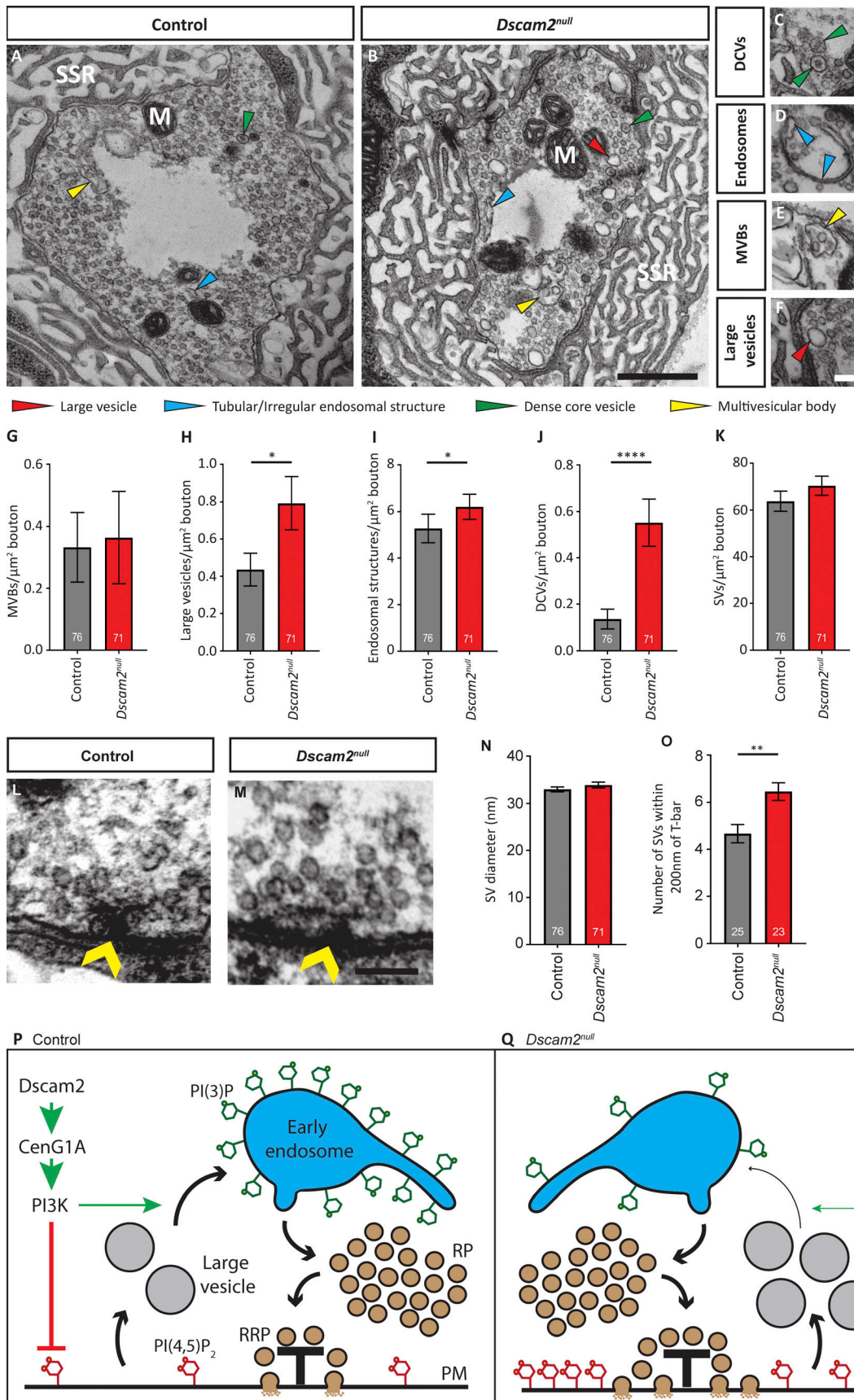


Figure 5. **Depletion of PI(3)P at *Dscam2* mutant motor neuron terminals.** **(A–D')** Representative images of Ib and Is axon terminals from control (*OK6-GAL4/UAS-2xFYVE-myc-GFP; +*) and *Dscam2<sup>null</sup>* (*OK6-GAL4/UAS-2xFYVE-myc-GFP; Dscam2<sup>null</sup>/Dscam2<sup>null</sup>*) labeled with HRP (magenta) and anti-GFP (green, A'–D') to visualize the early endosome marker (2xFYVE-GFP) under resting conditions (A–B') and following stimulation with 90 mM KCl (C–D'). Scale bars, 5 μm. **(E and E')** Quantification of 2xFYVE-GFP immunofluorescence intensity per bouton normalized to resting control for Ib (E) and Is (E'; Ib and Is analyzed with two-way ANOVA; groups within conditions compared with Sidak's post-test). **(F and G)** Representative images of FM4-64 labeling (gray) of axon terminals in control (F) and *Dscam2<sup>null</sup>* (G) larvae loaded by stimulation with 90 mM KCl HL3 for 1 min. Scale bar, 5 μm. **(H and H')** Quantification of FM4-64 fluorescence intensity relative to control for Ib (H) and Is (H'; unpaired Student's t test). Data shown as mean ± SEM; n indicated in graph. \*, P < 0.05 for all panels. IF, immunofluorescence.



**Figure 6. Ultrastructural analysis of *Dscam2<sup>null</sup>* boutons reveals endosomal defects. (A and B)** Representative electron micrographs of control (A) and *Dscam2<sup>null</sup>* (B) boutons. Arrowheads indicate examples of large vesicles (red), tubular endosomes (blue), DCVs (green), and MVBs (yellow). Mitochondria (M) and SSR indicated in white text. Scale bar, 500 nm. **(C–F)** High-magnification representative images of DCVs (green arrowheads, C), tubular endosomes (blue arrowheads, D), MVBs (yellow arrowhead, E), and large vesicles (red arrowhead, F). Scale bar, 100 nm. **(G–K)** Quantification of MVBs (G), large vesicle density (H), tubular endosome density (I), DCVs (J), and synaptic vesicle (SV) density (K). All measurements are the average per bouton. **(L and M)** Representative electron micrographs of control (L) and *Dscam2<sup>null</sup>* (M) synaptic vesicles surrounding active zones (T-bars indicated by yellow arrowheads). Scale bar, 100 nm. **(N and O)** Quantification of SV diameter (N) and the number of SVs within 200 nm of T-bar (O). **(P)** Model. In wild-type nerve terminals, *Dscam2* regulates CenG1A, which in turn enhances PI3K activity. This promotes PI(3)P deposition (green inositol ring) on early endosome (blue) membrane and inhibits the deposition of synaptic vesicles (brown) at active zones. Magenta inositol rings, PIP<sub>2</sub>; RP, releasable pool; RRP, readily releasable pool. **(Q)** In *Dscam2* mutants, decreases in CenG1A and PI3K activity lead to an increase in PIP<sub>2</sub> at the plasma membrane (magenta inositol ring) and a decrease in PI(3)P on early endosome (blue) membranes. Endosomal intermediates accumulate as 70–80-nm vesicles (gray), and more synaptic vesicles (brown) are deposited at active zones, which increases neurotransmitter release. Note that these pathways appear to function primarily under conditions of moderate neuronal activity. Data shown as mean  $\pm$  SEM; *n* indicated in graph; Mann–Whitney rank-sum test. \*, *P* > 0.05; \*\*, *P* < 0.01; \*\*\*\*, *P* < 0.0001 for all panels.

vesicle density and size was not different between control and *Dscam2<sup>null</sup>* (Fig. 6, K and N), consistent with the lack of mEJP frequency and amplitude phenotypes in mutant animals. Interestingly, however, we observed an  $\sim$ 40% increase in the number of synaptic vesicles within 200 nm of active zones in *Dscam2<sup>null</sup>* animals relative to control (Fig. 6, L, M, and O). An increase in the number of vesicles around release sites has been shown to correlate with increased quantal content at *Drosophila* synapses (Bruckner et al., 2012). To confirm this finding in a different *Dscam2* background, we also analyzed the single isoform lines. Given that *Dscam2A*, but not *Dscam2B*, larvae exhibited an increase in EJP', we expected that the former would have more synaptic vesicles at active zones whereas the latter would be similar to control. This is indeed what we observed (Fig. S4, O, P, and R). We conclude that *Dscam2* suppresses synaptic strength through a PI3K-dependent endosomal pathway that reduces the number of synaptic vesicles at active zones.

## Discussion

Cell recognition molecules play a crucial role in wiring the brain, but a major challenge is to understand how they promote and maintain specific connections between different neurons. One way to generate diversity in cell recognition molecules is through alternative splicing, which can produce distinct proteins from the same gene. These alternative protein isoforms can then provide distinct functions in different cell types (Aoto et al., 2013; Lah et al., 2014; Fuccillo et al., 2015). Here, we report that *Drosophila* *Dscam2*, a cell recognition molecule classically associated with axonal tiling and self-recognition during development, functions in regulating intimate facets of synaptic function. Only one of its two extracellular isoforms can carry out this function. Our results reveal that *Dscam2B* suppresses synaptic strength through a PI3K-dependent endosomal pathway that inhibits the number of synaptic vesicles at active zones.

Because the two isoforms of *Dscam2* differ at a single immunoglobulin domain that confers homophilic binding specificity, we originally hypothesized that these proteins would have similar functions in different cells. If this is the case, then both of the single isoform lines, which express one isoform of *Dscam2* in all *Dscam2*-positive cells, should generate similar phenotypes. This is what we observed for mEJP effects and NMJ morphology,

consistent with our previous analysis in the visual system (Lah et al., 2014). For example, lamina neurons L1 and L2 express distinct *Dscam2* isoforms, and their axon terminals contact each other. When these cells express the same isoform of *Dscam2*, axon terminal size decreases significantly, presumably due to inappropriate homophilic repulsion (Lah et al., 2014). Analogous relationships between neurons in the VNC likely exist. For example, sensory neurons that express *Dscam2B* could provide input into interneurons expressing *Dscam2A*, which in turn connect with motor neurons that express *Dscam2B*. If pre- and postsynaptic cells repelled each other, this simple circuit would be severely disrupted in the single isoform lines. However, other mechanisms are also possible, and demonstrating that inappropriate repulsion drives these gain-of-function phenotypes will require high-resolution circuit analysis within the VNC.

What then, is the role of *Dscam2* in the neurons of these simple circuits? It likely functions as a repulsive cue to maintain boundaries between neighboring neurons expressing the same *Dscam2* isoform as the larvae grow and may also act as a self-avoidance cue to help dendritic and axonal arbors maximize their coverage as they increase in size. Adhesive roles for the two isoforms are also possible, and each of these functions has been previously observed in the visual system (Millard et al., 2007; Millard et al., 2010; Lah et al., 2014; Tadros et al., 2016).

In contrast to the gain-of-function effects described above, the loss-of-function synaptic effects in *Dscam2<sup>null</sup>* and *Dscam2A* animals were unexpected and delineate a functional dichotomy between the two isoforms. How *Dscam2B*, but not *Dscam2A*, can suppress synaptic strength in motor neurons is currently a mystery. One possibility is that alternative *Dscam2* cytoplasmic domains, with unique signaling properties, are required for regulating synaptic strength. Seven different cytoplasmic variants of *Dscam2*, produced through a combination of alternative splicing and stop codon suppression (Jungreis et al., 2011), have been identified at the mRNA level using techniques such as RNA-sequencing (Graveley et al., 2011), but whether they are expressed at the protein level is not known. We deem it unlikely that a subset of these variants is specifically expressed in motor neurons to regulate synaptic strength, as their splicing would need to be intimately coordinated with that of isoform B (presumably through the splicing factor Muscleblind). We previously analyzed this using semi-quantitative RT-PCR and found

no evidence for changes in expression of the *Dscam2* cytoplasmic isoforms in *muscleblind* mutant animals (Li and Millard, 2019). In addition, most of the flanking sequences that likely regulate cell-specific splicing of exons 10A and 10B were removed in the single isoform lines (Lah et al., 2014), which would perturb coordination between Muscleblind and the selection of the specific cytoplasmic exons. Thus, although a subset of these cytoplasmic tails may transmit the signal that regulates synaptic strength, it is unlikely that a specific variant is linked to Dscam2B. A second, more likely possibility is that the functional differences between isoforms are dependent on the variable immunoglobulin domain. Since Dscam2 is not expressed in muscle, Dscam2 homophilic interactions between the motor neuron terminal and muscle cannot regulate synaptic strength. However, an alternative ligand that binds specifically to Dscam2B could either induce or suppress Dscam2 signaling within motor neurons. Secreted or membrane-bound cues may interact specifically with Dscam2B, although no alternative Dscam2 ligands were found in an in vitro screen with other cell recognition molecules (Özkan et al., 2013). A coreceptor that binds to Dscam2B, but not Dscam2A, in cis is another realistic possibility. In this scenario, the ligand for the coreceptor could be regulating Dscam2 signaling. Future studies to identify Dscam2-interacting proteins are required to resolve this issue. Finally, although our phenotypes strongly suggest that Dscam2 is functioning in the axon terminal, we have been unable to detect it in this compartment using antibodies. It is therefore possible that Dscam2 suppresses synaptic strength from the dendritic compartment of the motor neuron, although we deem this unlikely.

The mechanism through which Dscam2 regulates synaptic strength is remarkably specific and requires one of its two extracellular isoforms. Removal of *Dscam2* results in increased evoked, but not spontaneous, neurotransmitter release. Similar effects have been observed following modulation of endosomal regulators. For example, Rab5 levels are rate-limiting for synaptic strength, and loss of the GTPase-activating protein Skywalker (Sky) increases synaptic strength at the *Drosophila* larval NMJ (Wucherpennig et al., 2003; Uytterhoeven et al., 2011). Both Rab5 and *sky* mutants have overlapping phenotypes with *Dscam2* mutants. For example, large (70–80 nm) vesicles accumulate in all three of these mutants. However, in *sky* null NMJs, this is only observed in nerve terminals that have been stimulated (Uytterhoeven et al., 2011). A change in synaptic strength is another common theme. Both *sky* and *Dscam2* mutants exhibit an increase in evoked, but not spontaneous, release. In motor neurons expressing a dominant negative Rab5 (Rab5S43N), spontaneous release is also normal and there is a decrease in evoked release. In contrast, overexpression of Rab5 leads to increased evoked release (Wucherpennig et al., 2003), demonstrating that it is rate-limiting and likely a major target of regulation. Given that Rab5 binds to PI(3)P (Gillooly et al., 2003), a product of PI3K, Dscam2 and CenG1A have the ability to modulate Rab5 on membranes. Similarities in SV pools are also observed in these mutants. We observed more synaptic vesicles at active zones in the *Dscam2* mutants, and there is an increase in the releasable pool of synaptic vesicles in *sky* mutants (Uytterhoeven et al., 2011). This was not measured

directly for Rab5 overexpression, but docked vesicles and spontaneous release were unchanged in these animals (Wucherpennig et al., 2003), leading the authors to postulate increased pools of releasable vesicles at these NMJs.

The model of how *sky* mutants increase synaptic strength is by increasing traffic through the endosomal system, which results in younger synaptic proteins and consequently more fusogenic vesicles (Fernandes et al., 2014). Our data demonstrate that regulation of PI3K plays a critical role in this process, which is consistent with the dependence of endosomal sorting on specific phosphoinositides (Jähne et al., 2015). Dscam2 is necessary for promoting PI3K activity, and it carries out this function through CenG1A. Consistent with this, *Dscam2* mutants and *CenG1A* mutants exhibit increases in PIP<sub>2</sub>, a major substrate of PI3K. The accumulation of large vesicles in the *Dscam2* mutants combined with the decrease in PI(3)P in NMJs at rest suggest that fusion between endosome intermediates and the early endosome is impaired. How this leads to increased traffic through the endosomal pathway is unclear, as we would expect it to have the opposite effect. One possibility is that an impairment in endosomal fusion reduces the number of SV proteins traveling through the endosome compartment, and the neuron compensates by increasing the number of de novo synthesized SV proteins that traffic to the terminal. These young synaptic vesicle proteins then become incorporated into new vesicles and trafficked to the releasable pool.

Another difference between *Dscam2* and *sky* mutants (Fernandes et al., 2014; Uytterhoeven et al., 2011) is that the *Dscam2* phenotypes occur in unstimulated neurons, where demands on synaptic vesicle recycling are less than in KCl- or high frequency-stimulated preparations. It is possible that Dscam2 regulates the endosomal pathway in a PI3K-dependent manner under moderate levels of activity. Following large increases in synaptic vesicle release, bulk endocytic pathways contribute significantly to membrane recovery and collaborate with endosome recycling pathways (Cousin, 2009). Under these conditions, Dscam2 would either be inhibited or irrelevant due to the activation of alternative mechanisms that rapidly produce synaptic vesicles. This could explain the recovery of PI(3)P labeling in activated *Dscam2* mutant terminals (Fig. 5 E).

In conclusion, we have demonstrated that Dscam2 regulates neurophysiology through two distinct mechanisms. The first comprises regulated isoform expression in different cell types that presumably involves the spatial organization of neurites through isoform-specific homophilic interactions, as has been described previously (Millard et al., 2007; Lah et al., 2014; Tadros et al., 2016). The second mechanism, which decreases synaptic strength in motor neurons, is isoform specific. Dscam2B decreases neurotransmitter release in motor neuron terminals by inhibiting the number of synaptic vesicles that get trafficked to active zones through a PI3K-dependent endosomal pathway (Fig. 6, P and Q). Our study demonstrates how cell-specific expression of protein isoforms can provide unique functions to different cells and thus explains how an incredibly complex organ like the brain can operate effectively using a small toolkit of genes.

## Materials and methods

### *Drosophila melanogaster* rearing and staging details

Flies were reared at room temperature (22–25°C) and humidity on standard cornmeal medium. The following lines were acquired from Bloomington *Drosophila* Stock Centre: *CenGIA<sup>EY01217</sup>* (15502), *Lat<sup>6</sup>* (5571), *Leo<sup>12BL</sup>* (9572), *Psn<sup>143</sup>* (8297), *Df(2L)BSC6* (6338), *Df(2L)BSC105* (8671), *Df(2L)BSC694* (26546), *Df(2L)Exel7080* (7853), *Df(3L)BSC669* (26521), *Df(3L)BSC671* (26523), *Df(3L)Exel6092* (7571), *elav-GAL4* (8765), *nSyb-GAL4*, *OK6-GAL4* (64199), *OK371-GAL4* (26160), *UAS-Dscam2-RNAi* (51839), *UAS-mCD8::GFP* (5137), *UAS-PLCδPH-mCherry* (51658), and *UAS-2xFYVE-myc-GFP* (42712). The following fly lines were generated in the Millard laboratory and have been previously described: *Dscam2<sup>null-1</sup>* and *Dscam2<sup>null-3</sup>* (Millard et al., 2007), *Dscam2A-GAL4*, and *Dscam2B-GAL4* (Lah et al., 2014). All animals selected for experiments were on a *w<sup>1118</sup>* background, and larvae of either sex were selected only if in wandering third-instar stage. Experiments used larvae and embryos raised at 25°C unless otherwise specified. Embryos of either sex were staged to within a 2-h window.

### Larval ex vivo fillet preparation and embryo dissection

Dissections of third-instar larvae were performed in hemolymph-like 3 (HL3) saline (Stewart et al., 1994) following the magnetic body-wall muscle procedure described in Ramachandran and Budnik (2010). In brief, an incision was made along the dorsal length of third-instar larvae, and the body wall was pinned open to expose internal organs and musculature. Organs were carefully removed, taking care not to damage the underlying muscles, and if required, peripheral nerves were cut to remove the brain. Bath [Ca<sup>2+</sup>] was dependent on the type of assay performed.

Stage 16 embryos were manually dechorionated and devitelinated by gently rolling on doubled-sided tape. They were then transferred to a drop of HL3 on a glass slide and filleted using sharp glass capillaries created using a model P-97 puller (Sutter Instruments) by taking advantage of the adhesion between stage 16 embryo cuticle and glass. Embryos were fixed, stained, and imaged on the same glass slide.

### Immunohistochemistry

Dissected third-instar larval fillets were fixed in PBS containing 4% PFA (wt/vol) for 20 min for all antibody combinations used with the exception of GluRIIA, which required fixation in 100% methanol for 5 min. Following fixation, immunohistochemistry was performed as previously described (Brent et al., 2009). Fixed filleted larvae were first washed in PBS, then incubated in blocking buffer for 1 h at room temperature. Blocking buffer consisted of PBS containing 5% goat serum and 0.5% Triton-X. Following this, the filleted larvae were incubated in blocking buffer containing primary antibodies overnight at 4°C. Antibody dilutions were used as follows: Cy3-conjugated anti-HRP (1:500; 123-165-021; Jackson ImmunoResearch Laboratories); mouse anti-brp (1:100, nc82; Developmental Studies Hybridoma Bank [DSHB]); mouse anti-dlg (1:500, 4F3; DSHB), mouse anti-GFP (1:500, 4745-1051; Bio-Rad), mouse anti-Synapsin (anti-Syn; 1:100, 3C11; DSHB), mouse anti-GluRIIA (1:100, MH2B; DSHB), mouse

anti-Syt1 (1:100, 3H2 2D7; DSHB), and Alexa Fluor 568 Phalloidin (1:500, A12381; Thermo Fisher Scientific). After incubating with primary antibodies overnight, filleted larvae were washed in PBS and then incubated in blocking buffer containing secondary antibodies overnight at 4°C. Secondary antibodies used included Alexa Fluor 488-conjugated goat anti-mouse IgG (1:800, A-11001; Thermo Fisher Scientific) and Alexa Fluor 647-conjugated goat anti-mouse IgG (1:800, A28181; Thermo Fisher Scientific). Antibody incubations were performed overnight at 4°C. Lastly, after incubating with secondary antibodies, filleted larvae were washed in PBS and mounted onto glass slides in glycerol.

### FM4-64 dye labeling

For FM4-64 experiments, methods according to Verstreken et al. (2008) were closely followed. In brief, larvae were dissected in Ca<sup>2+</sup>-free HL3 and then incubated with HL3 containing 90 mM KCl and FM4-64FX (4 μM, F34653; Thermo Fisher Scientific) for 1 min. Following this, larvae were washed rigorously by alternating positive and negative pressure with fresh Ca<sup>2+</sup>-free HL3 in bath over 5 min and at least three solution changes. Preparations were then fixed, mounted on glass slides in glycerol, and imaged within 24 h.

### Image acquisition of stained preparations and image quantification

Microscopy was performed at the School of Biomedical Sciences Imaging Facility and Queensland Brain Institute Advanced Microscopy Facility. Imaging of larval preparations was predominantly performed on an Olympus FV1000 upright scanning confocal microscope with NA 1.35 60× or NA 1.4 100× oil immersion objectives via photomultiplier tubes at room temperature. Fluoview software (Olympus America Inc.) was used to acquire images taken on the FV1000 system. Imaging was also performed on an Axio Observer Z1 (Zeiss) equipped with a CSU-W1 spinning-disk head (Yokogawa Corporation of America), ORCA-Flash4.0 v2 sCMOS camera (Hamamatsu Photonics), and NA 1.4 100× oil immersion objective. Huygens software (Scientific Volume Imaging) was used to acquire images taken on the spinning-disk system. Optical sectioning and laser settings were kept constant across all image data acquisition sessions for like experiments and depended on the type of experiment being performed. Images were taken from NMJs formed upon muscles 6 and 7 by MN6/7-Ib and MNSNb/d-Is in abdominal segments 3 and 4 (A3 and A4). No more than two NMJs were imaged per larva.

Analysis of all images was done using ImageJ (National Institutes of Health). To measure the number of boutons per NMJ, anti-Syn immunoreactivity was used to label individual boutons, which were manually counted. To measure the maximal cross-sectional area of muscles, a perimeter was traced around the perpendicular muscle cross section from maximal z-stack projections of phalloidin. Cross-sectional muscle area was then calculated from the traced perimeters. To measure bouton and subsynaptic reticulum (SSR) diameters, a line was drawn across the longest axis perpendicular to the main branch of HRP and anti-dlg immunoreactivity from maximal z-stack projections. All boutons on at least one Ib or Is branch per NMJ were

measured and averaged to generate representative values. To measure GluRIIA fluorescence intensity, HRP immunostaining was used to generate “synaptic” regions of interest (ROIs) from which raw anti-GluRIIA pixel intensity was measured. Three random regions of similar cross-sectional area that did not intersect with synaptic ROIs were then determined as “non-synaptic” ROIs and were averaged to determine the background fluorescence. The synaptic GluRIIA raw pixel values were then divided by nonsynaptic pixel values to generate normalized GluRIIA fluorescence values. These results were confirmed by manually measuring the size and average pixel values of at least 20 individual GluRIIA puncta per NMJ for every animal. A similar approach was taken for measuring relative Syt1 immunofluorescence intensity with the exception of having to define and measure puncta, as Syt1 immunoreactivity filled the entire bouton.

Measurement of PLC $\delta$ PH-mCherry and 2xFYVE-GFP average pixel intensity per bouton was performed using ROIs that were made by drawing perimeters around HRP-positive boutons. For these genotypes, immunostaining was performed to amplify signals of the tags. The same methodology was used to quantify FM4-64FX immunofluorescence intensity, but ROIs were generated based on the FM4-64FX signal directly, instead of from HRP.

#### Transmission electron microscopy and analysis of micrographs

Dissected larvae were fixed in 4% PFA and 2.5% glutaraldehyde solution overnight. After a PBS rinse, the samples were stained with 1% osmium tetroxide and 2% uranyl acetate using a Pelco Biowave. They were then dehydrated in ethanol series (50%–100%) followed by infiltration with increasing concentrations of epon resin (25%–100%), in which they were left immersed for 24 h at room temperature. Samples were subsequently processed in the resin with the Biowave high vacuum function before being embedded in fresh resin and polymerized in a 60°C oven for 48 h. Formvar-coated, one-slot grids were used to collect thin sections (50 nm) obtained via a Leica Ultracut UC6 Ultramicrotome by taking transverse sections of muscles at intervals of 2.5  $\mu$ m over 35–150  $\mu$ m. Sections were then post-stained using Reynold’s lead citrate solution and 4% uranyl acetate. Boutons were photographed with a JEOL 1011 electron microscope at 80 kV. ImageJ was used to quantify substructures from electron micrographs in a blinded manner.

We quantified several parameters including bouton size; SSR size; and number of mitochondria, dense core vesicles, MVBs, synaptic vesicles, large endosomal vesicles, tubular/irregular structures, and multimembranous structures. Mitochondria were defined by the presence of cristae and double outer membranes. DCVs were defined by the presence of circular-shaped electron dense material enclosed by a single membrane. MVBs were defined by the presence of multiple (more than one) clear membrane-bound objects within a single clear membrane-bound object. Multimembranous structures were defined by multiple (more than one) lamellar-appearing membranes enclosing a clear core.

To define and measure the size of synaptic vesicles, large endosomal vesicles, and tubular/irregular endosomes in micrographs, we drew perimeters around all clear, membrane-bound

structures within boutons. Of these structures, synaptic vesicles were defined as having circularity values  $>0.75$ , aspect ratios  $<2$ , and diameters  $<70$  nm. Large vesicles were defined as having circularity values  $>0.75$ , aspect ratios  $<2$ , and diameters  $>70$  nm. Tubular/irregular structures were defined as structures with circularity values  $<0.75$  and aspect ratios  $>2$ . Multi-membranous structures were identified by the presence of at least one membrane-bound structure within another membrane-bound structure.

#### Intracellular recordings of larval muscle fibers

Larvae were dissected in HL3 containing variable  $[Ca^{2+}]$  depending on the type of assay being performed. All peripheral nerve bundles were severed, and the central nervous system was removed. Muscle 6 in A3 or A4 was chosen for impalement using thick-walled, high-resistance (80–100 M $\Omega$ ), sharp borosilicate electrodes filled with a 2:1 ratio of 3 M KCH<sub>3</sub>COO and 3 M KCl. Impaled muscles were left unstimulated until the resting membrane potential reached stability, as defined by fluctuations of  $<10\%$  within 5 min. Floating ends of the severed nerve bundles were recruited using wide-tipped (10–12  $\mu$ m) thin-walled borosilicate electrodes containing HL3 (Kurdyak et al., 1994). Synaptic responses were elicited by stimulating recruited nerves with 0.3-ms-long square wave pulses at a frequency of 0.5–1 Hz using a SD9 square pulse stimulator (Grass Instruments). Spontaneous mEJPs were recorded for no less than 3 min, and EJPs were recorded for 1–2 min. No more than two muscles were recorded per larva. All intracellular responses were digitized using the LabChart 7.0 software (AD Instruments) at a sampling rate of 40 kHz and were amplified using an Axoclamp 2B amplifier (Molecular Devices), direct current (DC) high-pass Bessel, and 3-kHz low-pass Bessel. All EJPs and mEJPs were measured manually in LabChart7.

EJP amplitudes were corrected for nonlinear summation as described by Martin (1976) and elaborated upon by McLachlan and Martin (1981). Quantal content was calculated by dividing average EJP amplitude corrected for nonlinear summation (EJP’) by average mEJP amplitude for control and *Dscam2<sup>null</sup>* recordings. For *Dscam2* single isoform recordings, average EJP’ amplitude was instead divided by median mEJP amplitude since most individual frequency-amplitude histograms revealed skewed distributions. Amplitude-variation plots were generated by fitting standard quadratic equations to plotted values of average, SEM, and n for EJP’ amplitude and trial-to-trial variation of EJP’ per  $[Ca^{2+}]_o$  explored.

#### PI3K inhibitor experiments

Wortmannin (19545–26-7; Sigma-Aldrich) and LY294002 (S1105; Selleck Chemicals) stocks were dissolved in DMSO and maintained at  $-20^\circ\text{C}$ . For experiments, drugs in DMSO were dissolved into HL3 solution up to 24 h before use and stored at  $4^\circ\text{C}$ . Larvae were dissected in drug-free HL3 and then incubated with Wortmannin (1 h) or LY294002 (30 min) before recordings. Total DMSO in HL3 did not exceed 0.001% (vol/vol).

#### Statistical analyses

GraphPad Prism 7 was used to perform all analyses and generate graphs. The D’Agostino–Pearson omnibus test for normality was

used to test whether or not data assumed a Gaussian distribution unless the number of values collected was too small, in which case the Shapiro–Wilk test for normality was used instead. To determine statistical significance between groups that all assumed Gaussian distributions, parametric tests were employed (unpaired Student's *t* test, one-way ANOVA with Tukey's multiple comparisons, and two-way ANOVA with Sidak's multiple comparisons). To determine statistical significance between groups in which at least one population did not assume a Gaussian distribution, nonparametric tests were employed instead (Mann–Whitney rank-sum test, Kruskal–Wallis test with Dunn's multiple comparison, and two-way ANOVA with Sidak's multiple comparisons). Significance was determined at  $P < 0.05$ . All error bars represent average  $\pm$  SEM. Numbers (*n*) indicated in graphs or figure legends represent number of NMJs analyzed. No more than two NMJs were taken per larva.

### Online supplemental material

**Fig. S1** shows expression of *Dscam2B* in a larval abdominal hemisegment. It also shows expression of *Dscam2A* and *Dscam2* throughout embryonic development. **Fig. S2** shows extended electrophysiological analyses of those presented in **Fig. 2**. **Fig. S3** shows analysis of *dlg* and *Syt1* fluorescence intensity and the results from a genetic interaction screen against *Dscam2<sup>null</sup>* heterozygotes using EJC amplitude as a readout. **Fig. S4** shows analysis of electron micrographs taken from *Dscam2* single A and B isoform larvae in extension of the results shown in **Fig. 6**. Table S1 shows known properties of all larval abdominal segment motor neurons including expression of *Dscam2B*.

### Acknowledgments

We thank Yong Qi Lin and Shanker Karunanithi for their technical assistance with neuromuscular synaptic recordings; Erica Lovas, Kathryn Green, and Matthias Floetenmeyer for providing electron microscopy technical assistance; and Frederic Meunier (University of Queensland, Brisbane, Australia) for generously providing the FM styryl dyes.

G. Lorenzo Odierna was supported by an Australian Postgraduate Award, and project funding was provided by a National Health and Medical Research Council grant to S. Sean Millard (APP1105792).

Author contributions: G. Lorenzo Odierna performed all experiments and analyzed all data with the exception of electron microscopy data collection by L.E. Harris and CenG1A PLC $\delta$ PH-mCherry data collection and analysis by S.K. Kerwin. G. Lorenzo Odierna and S. Sean Millard wrote the manuscript, P.G. Noakes provided reagents and expertise for the EM experiments. G.J. Shin provided critical feedback on the manuscript, S. Sean Millard secured funding and provided reagents, and P.G. Noakes, N.A. Lavidis, and S. Sean Millard provided expertise.

The authors declare no competing financial interests.

Submitted: 24 September 2019

Revised: 19 February 2020

Accepted: 5 March 2020

### References

- Almén, M.S., K.J. Nordström, R. Fredriksson, and H.B. Schiöth. 2009. Mapping the human membrane proteome: a majority of the human membrane proteins can be classified according to function and evolutionary origin. *BMC Biol.* 7:50. <https://doi.org/10.1186/1741-7007-7-50>
- Aoto, J., D.C. Martinelli, R.C. Malenka, K. Tabuchi, and T.C. Südhof. 2013. Presynaptic neuexin-3 alternative splicing trans-synaptically controls postsynaptic AMPA receptor trafficking. *Cell.* 154:75–88. <https://doi.org/10.1016/j.cell.2013.05.060>
- Baines, R.A., and M. Bate. 1998. Electrophysiological development of central neurons in the *Drosophila* embryo. *J. Neurosci.* 18:4673–4683. <https://doi.org/10.1523/JNEUROSCI.18-12-04673.1998>
- Brent, J., K. Werner, and B.D. McCabe. 2009. *Drosophila* larval NMJ immunohistochemistry. *J. Vis. Exp.* (25):1108.
- Broadie, K., and M. Bate. 1993. Innervation directs receptor synthesis and localization in *Drosophila* embryo synaptogenesis. *Nature.* 361:350–353. <https://doi.org/10.1038/361350a0>
- Bruckner, J.J., S.J. Gratz, J.K. Slind, R.R. Geske, A.M. Cummings, S.E. Galindo, L.K. Donohue, and K.M. O'Connor-Giles. 2012. Fife, a *Drosophila* Piccolo-RIM homolog, promotes active zone organization and neurotransmitter release. *J. Neurosci.* 32:17048–17058. <https://doi.org/10.1523/JNEUROSCI.3267-12.2012>
- Chan, C.B., and K. Ye. 2012. Phosphoinositide 3-kinase enhancer (PIKE) in the brain: is it simply a phosphoinositide 3-kinase/Akt enhancer? *Rev. Neurosci.* 23:153–161. <https://doi.org/10.1515/revneuro-2011-0066>
- Cooper, L.N., and M.F. Bear. 2012. The BCM theory of synapse modification at 30: interaction of theory with experiment. *Nat. Rev. Neurosci.* 13: 798–810. <https://doi.org/10.1038/nrn3353>
- Cousin, M.A. 2009. Activity-dependent bulk synaptic vesicle endocytosis—a fast, high capacity membrane retrieval mechanism. *Mol. Neurobiol.* 39: 185–189. <https://doi.org/10.1007/s12035-009-8062-3>
- Cousin, M.A., C.S. Malladi, T.C. Tan, C.R. Raymond, K.J. Smillie, and P.J. Robinson. 2003. Synapsin I-associated phosphatidylinositol 3-kinase mediates synaptic vesicle delivery to the readily releasable pool. *J. Biol. Chem.* 278:29065–29071. <https://doi.org/10.1074/jbc.M302386200>
- del Castillo, J., and B. Katz. 1954a. Quantal components of the end-plate potential. *J. Physiol.* 124:560–573. <https://doi.org/10.1113/jphysiol.1954.sp005129>
- del Castillo, J., and B. Katz. 1954b. Statistical factors involved in neuromuscular facilitation and depression. *J. Physiol.* 124:574–585. <https://doi.org/10.1113/jphysiol.1954.sp005130>
- Delvendahl, I., and M. Müller. 2019. Homeostatic plasticity—a presynaptic perspective. *Curr. Opin. Neurobiol.* 54:155–162. <https://doi.org/10.1016/j.conb.2018.10.003>
- Dudel, J., and S.W. Kuffler. 1961. Mechanism of facilitation at the crayfish neuromuscular junction. *J. Physiol.* 155:530–542. <https://doi.org/10.1113/jphysiol.1961.sp006645>
- Fernandes, A.C., V. Uytterhoeven, S. Kuenen, Y.C. Wang, J.R. Slabbaert, J. Swerts, J. Kaspruwicz, S. Aerts, and P. Verstreken. 2014. Reduced synaptic vesicle protein degradation at lysosomes curbs TBCLD24/sky-induced neurodegeneration. *J. Cell Biol.* 207:453–462. <https://doi.org/10.1083/jcb.201406026>
- Frank, C.A. 2014. Homeostatic plasticity at the *Drosophila* neuromuscular junction. *Neuropharmacology.* 78:63–74. <https://doi.org/10.1016/j.neuropharm.2013.06.015>
- Fucillo, M.V., C. Földy, Ö. Gökce, P.E. Rothwell, G.L. Sun, R.C. Malenka, and T.C. Südhof. 2015. Single-Cell mRNA Profiling Reveals Cell-Type-Specific Expression of Neuexin Isoforms. *Neuron.* 87:326–340. <https://doi.org/10.1016/j.neuron.2015.06.028>
- Gillooly, D.J., C. Raiborg, and H. Stenmark. 2003. Phosphatidylinositol 3-phosphate is found in microdomains of early endosomes. *Histochem. Cell Biol.* 120:445–453. <https://doi.org/10.1007/s00418-003-0591-7>
- Gorvel, J.P., P. Chavrier, M. Zerial, and J. Gruenberg. 1991. rab5 controls early endosome fusion in vitro. *Cell.* 64:915–925. [https://doi.org/10.1016/0092-8674\(91\)90316-Q](https://doi.org/10.1016/0092-8674(91)90316-Q)
- Graveley, B.R., A.N. Brooks, J.W. Carlson, M.O. Duff, J.M. Landolin, L. Yang, C.G. Artieri, M.J. van Baren, N. Boley, B.W. Booth, et al. 2011. The developmental transcriptome of *Drosophila melanogaster*. *Nature.* 471: 473–479. <https://doi.org/10.1038/nature09715>
- Grenningloh, G., E.J. Rehm, and C.S. Goodman. 1991. Genetic analysis of growth cone guidance in *Drosophila*: fasciclin II functions as a neuronal recognition molecule. *Cell.* 67:45–57. [https://doi.org/10.1016/0092-8674\(91\)90571-F](https://doi.org/10.1016/0092-8674(91)90571-F)

- Gross, C., C.W. Chang, S.M. Kelly, A. Bhattacharya, S.M. McBride, S.W. Danielson, M.Q. Jiang, C.B. Chan, K. Ye, J.R. Gibson, et al. 2015. Increased expression of the PI3K enhancer PIKE mediates deficits in synaptic plasticity and behavior in fragile X syndrome. *Cell Rep.* 11: 727–736. <https://doi.org/10.1016/j.celrep.2015.03.060>
- Hauswirth, A.G., K.J. Ford, T. Wang, R.D. Fetter, A. Tong, and G.W. Davis. 2018. A postsynaptic PI3K- $\alpha$  dependent signaling controller for presynaptic homeostatic plasticity. *eLife.* 7:e31535. <https://doi.org/10.7554/eLife.31535>
- Helenius, A., I. Mellman, D. Wall, and A. Hubbard. 1983. Endosomes. *Trends Biochem. Sci.* 8:245–250. [https://doi.org/10.1016/0968-0004\(83\)90350-X](https://doi.org/10.1016/0968-0004(83)90350-X)
- Homma, M., S. Nagashima, T. Fukuda, S. Yanagi, H. Miyakawa, E. Suzuki, and T. Morimoto. 2014. Downregulation of Centaurin gammaA increases synaptic transmission at Drosophila larval neuromuscular junctions. *Eur. J. Neurosci.* 40:3158–3170. <https://doi.org/10.1111/ejn.12681>
- Howlett, E., C.C. Lin, W. Lavery, and M. Stern. 2008. A PI3-kinase-mediated negative feedback regulates neuronal excitability. *PLoS Genet.* 4: e1000277. <https://doi.org/10.1371/journal.pgen.1000277>
- Ishihara, H., Y. Shibasaki, N. Kizuki, H. Katagiri, Y. Yazaki, T. Asano, and Y. Oka. 1996. Cloning of cDNAs encoding two isoforms of 68-kDa type I phosphatidylinositol-4-phosphate 5-kinase. *J. Biol. Chem.* 271: 23611–23614. <https://doi.org/10.1074/jbc.271.39.23611>
- Jähne, S., S.O. Rizzoli, and M.S. Helm. 2015. The structure and function of presynaptic endosomes. *Exp. Cell Res.* 335:172–179. <https://doi.org/10.1016/j.yexcr.2015.04.017>
- Jan, L.Y., and Y.N. Jan. 1976. Properties of the larval neuromuscular junction in Drosophila melanogaster. *J. Physiol.* 262:189–214. <https://doi.org/10.1113/jphysiol.1976.sp011592>
- Jones, A.T., and M.J. Clague. 1995. Phosphatidylinositol 3-kinase activity is required for early endosome fusion. *Biochem. J.* 311:31–34. <https://doi.org/10.1042/bj3110031>
- Jungreis, I., M.F. Lin, R. Spokony, C.S. Chan, N. Negre, A. Victorsen, K.P. White, and M. Kellis. 2011. Evidence of abundant stop codon read-through in Drosophila and other metazoa. *Genome Res.* 21:2096–2113. <https://doi.org/10.1101/gr.119974.110>
- Kerwin, S.K., J.S.S. Li, P.G. Noakes, G.J. Shin, and S.S. Millard. 2018. Regulated Alternative Splicing of *Drosophila Dscam2* Is Necessary for Attaining the Appropriate Number of Photoreceptor Synapses. *Genetics.* 208:717–728. <https://doi.org/10.1534/genetics.117.300432>
- Kim, M.D., Y. Wen, and Y.N. Jan. 2009. Patterning and organization of motor neuron dendrites in the Drosophila larva. *Dev. Biol.* 336:213–221. <https://doi.org/10.1016/j.ydbio.2009.09.041>
- Kurdyak, P., H.L. Atwood, B.A. Stewart, and C.F. Wu. 1994. Differential physiology and morphology of motor axons to ventral longitudinal muscles in larval Drosophila. *J. Comp. Neurol.* 350:463–472. <https://doi.org/10.1002/cne.903500310>
- Lah, G.J., J.S. Li, and S.S. Millard. 2014. Cell-specific alternative splicing of Drosophila *Dscam2* is crucial for proper neuronal wiring. *Neuron.* 83: 1376–1388. <https://doi.org/10.1016/j.neuron.2014.08.002>
- Landgraf, M., T. Bossing, G.M. Technau, and M. Bate. 1997. The origin, location, and projections of the embryonic abdominal motorneurons of Drosophila. *J. Neurosci.* 17:9642–9655. <https://doi.org/10.1523/JNEUROSCI.17-24-09642.1997>
- Li, J.S.S., and S.S. Millard. 2019. Deterministic splicing of *Dscam2* is regulated by *Muscleblind*. *Sci. Adv.* 5:eaav1678.
- Lin, D.M., R.D. Fetter, C. Kopczyński, G. Grenningloh, and C.S. Goodman. 1994. Genetic analysis of Fasciclin II in Drosophila: defasciculation, refasciculation, and altered fasciculation. *Neuron.* 13:1055–1069. [https://doi.org/10.1016/0896-6273\(94\)90045-0](https://doi.org/10.1016/0896-6273(94)90045-0)
- Lynch, M.A. 2004. Long-term potentiation and memory. *Physiol. Rev.* 84: 87–136. <https://doi.org/10.1152/physrev.00014.2003>
- Martin, A.R. 1976. The effect of membrane capacitance on non-linear summation of synaptic potentials. *J. Theor. Biol.* 59:179–187. [https://doi.org/10.1016/S0022-5193\(76\)80031-8](https://doi.org/10.1016/S0022-5193(76)80031-8)
- McLachlan, E.M., and A.R. Martin. 1981. Non-linear summation of end-plate potentials in the frog and mouse. *J. Physiol.* 311:307–324. <https://doi.org/10.1113/jphysiol.1981.sp013586>
- Meinertzhagen, I.A., and S.D. O'Neil. 1991. Synaptic organization of columnar elements in the lamina of the wild type in Drosophila melanogaster. *J. Comp. Neurol.* 305:232–263. <https://doi.org/10.1002/cne.903050206>
- Menon, K.P., R.A. Carrillo, and K. Zinn. 2013. Development and plasticity of the Drosophila larval neuromuscular junction. *Wiley Interdiscip. Rev. Dev. Biol.* 2:647–670. <https://doi.org/10.1002/wdev.108>
- Meunier, F.A., S.L. Osborne, G.R.V. Hammond, F.T. Cooke, P.J. Parker, J. Domin, and G. Schiavo. 2005. Phosphatidylinositol 3-kinase C2alpha is essential for ATP-dependent priming of neurosecretory granule exocytosis. *Mol. Biol. Cell.* 16:4841–4851. <https://doi.org/10.1091/mbc.e05-02-0171>
- Millard, S.S., J.J. Flanagan, K.S. Pappu, W. Wu, and S.L. Zipursky. 2007. *Dscam2* mediates axonal tiling in the Drosophila visual system. *Nature.* 447:720–724. <https://doi.org/10.1038/nature05855>
- Millard, S.S., Z. Lu, S.L. Zipursky, and I.A. Meinertzhagen. 2010. Drosophila *dscam* proteins regulate postsynaptic specificity at multiple-contact synapses. *Neuron.* 67:761–768. <https://doi.org/10.1016/j.neuron.2010.08.030>
- Neuhaus-Follini, A., and G.J. Bashaw. 2015. The Intracellular Domain of the Frazzled/DCC Receptor Is a Transcription Factor Required for Commissural Axon Guidance. *Neuron.* 87:751–763. <https://doi.org/10.1016/j.neuron.2015.08.006>
- Nilsen, T.W., and B.R. Graveley. 2010. Expansion of the eukaryotic proteome by alternative splicing. *Nature.* 463:457–463. <https://doi.org/10.1038/nature08909>
- Özkan, E., R.A. Carrillo, C.L. Eastman, R. Weiszmann, D. Waghray, K.G. Johnson, K. Zinn, S.E. Celniker, and K.C. Garcia. 2013. An extracellular interactome of immunoglobulin and LRR proteins reveals receptor-ligand networks. *Cell.* 154:228–239. <https://doi.org/10.1016/j.cell.2013.06.006>
- Ramachandran, P., and V. Budnik. 2010. Dissection of Drosophila larval body-wall muscles. *Cold Spring Harb. Protoc.* 2010:pdb.prot5469. <https://doi.org/10.1101/pdb.prot5469>
- Schuster, C.M., G.W. Davis, R.D. Fetter, and C.S. Goodman. 1996. Genetic dissection of structural and functional components of synaptic plasticity. I. Fasciclin II controls synaptic stabilization and growth. *Neuron.* 17:641–654. [https://doi.org/10.1016/S0896-6273\(00\)80197-X](https://doi.org/10.1016/S0896-6273(00)80197-X)
- Shapiro, L., J. Love, and D.R. Colman. 2007. Adhesion molecules in the nervous system: structural insights into function and diversity. *Annu. Rev. Neurosci.* 30:451–474. <https://doi.org/10.1146/annurev.neuro.29.051605.113034>
- Stewart, B.A., H.L. Atwood, J.J. Renger, J. Wang, and C.F. Wu. 1994. Improved stability of Drosophila larval neuromuscular preparations in haemolymph-like physiological solutions. *J. Comp. Physiol. A Neuroethol. Sens. Neural Behav. Physiol.* 175:179–191. <https://doi.org/10.1007/BF00215114>
- Stewart, B.A., C.M. Schuster, C.S. Goodman, and H.L. Atwood. 1996. Homeostasis of synaptic transmission in Drosophila with genetically altered nerve terminal morphology. *J. Neurosci.* 16:3877–3886. <https://doi.org/10.1523/JNEUROSCI.16-12-03877.1996>
- Tadros, W., S. Xu, O. Akin, C.H. Yi, G.J. Shin, S.S. Millard, and S.L. Zipursky. 2016. *Dscam* Proteins Direct Dendritic Targeting through Adhesion. *Neuron.* 89:480–493. <https://doi.org/10.1016/j.neuron.2015.12.026>
- Tan, X., N. Thapa, S. Choi, and R.A. Anderson. 2015. Emerging roles of PtdIns(4,5)P<sub>2</sub>—beyond the plasma membrane. *J. Cell Sci.* 128:4047–4056. <https://doi.org/10.1242/jcs.175208>
- Thalhammer, A., and L.A. Cingolani. 2014. Cell adhesion and homeostatic synaptic plasticity. *Neuropharmacology.* 78:23–30. <https://doi.org/10.1016/j.neuropharm.2013.03.015>
- Thu, C.A., W.V. Chen, R. Rubinstein, M. Chevee, H.N. Wolcott, K.O. Felsevalyi, J.C. Tapia, L. Shapiro, B. Honig, and T. Maniatis. 2014. Single-cell identity generated by combinatorial homophilic interactions between  $\alpha$ ,  $\beta$ , and  $\gamma$  protocadherins. *Cell.* 158:1045–1059. <https://doi.org/10.1016/j.cell.2014.07.012>
- Thyagarajan, B., J.G. Potian, P. Baskaran, and J.J. McArdle. 2014. Capsaicin modulates acetylcholine release at the myoneural junction. *Eur. J. Pharmacol.* 744:211–219. <https://doi.org/10.1016/j.ejphar.2014.09.044>
- Uytterhoeven, V., S. Kuenen, J. Kasprovicz, K. Miskiewicz, and P. Verstreken. 2011. Loss of skywalker reveals synaptic endosomes as sorting stations for synaptic vesicle proteins. *Cell.* 145:117–132. <https://doi.org/10.1016/j.cell.2011.02.039>
- Verstreken, P., T. Ohyama, and H.J. Bellen. 2008. FM 1-43 labeling of synaptic vesicle pools at the Drosophila neuromuscular junction. *Methods Mol. Biol.* 440:349–369. [https://doi.org/10.1007/978-1-59745-178-9\\_26](https://doi.org/10.1007/978-1-59745-178-9_26)
- Verstreken, P., T. Ohyama, C. Haueter, R.L. Habets, Y.Q. Lin, L.E. Swan, C.V. Ly, K.J. Venken, P. De Camilli, and H.J. Bellen. 2009. Tweek, an

- evolutionarily conserved protein, is required for synaptic vesicle recycling. *Neuron*. 63:203–215. <https://doi.org/10.1016/j.neuron.2009.06.017>
- Watanabe, S., and E. Boucrot. 2017. Fast and ultrafast endocytosis. *Curr. Opin. Cell Biol.* 47:64–71. <https://doi.org/10.1016/j.ccb.2017.02.013>
- Watanabe, S., Q. Liu, M.W. Davis, G. Hollopeter, N. Thomas, N.B. Jorgensen, and E.M. Jorgensen. 2013a. Ultrafast endocytosis at *Caenorhabditis elegans* neuromuscular junctions. *eLife*. 2:e00723. <https://doi.org/10.7554/eLife.00723>
- Watanabe, S., B.R. Rost, M. Camacho-Pérez, M.W. Davis, B. Söhl-Kielczynski, C. Rosenmund, and E.M. Jorgensen. 2013b. Ultrafast endocytosis at mouse hippocampal synapses. *Nature*. 504:242–247. <https://doi.org/10.1038/nature12809>
- Wucherpfennig, T., M. Wilsch-Bräuninger, and M. González-Gaitán. 2003. Role of *Drosophila* Rab5 during endosomal trafficking at the synapse and evoked neurotransmitter release. *J. Cell Biol.* 161:609–624. <https://doi.org/10.1083/jcb.200211087>
- Yang, Y., and N. Calakos. 2013. Presynaptic long-term plasticity. *Front. Synaptic Neurosci.* 5:8. <https://doi.org/10.3389/fnsyn.2013.00008>

Supplemental material

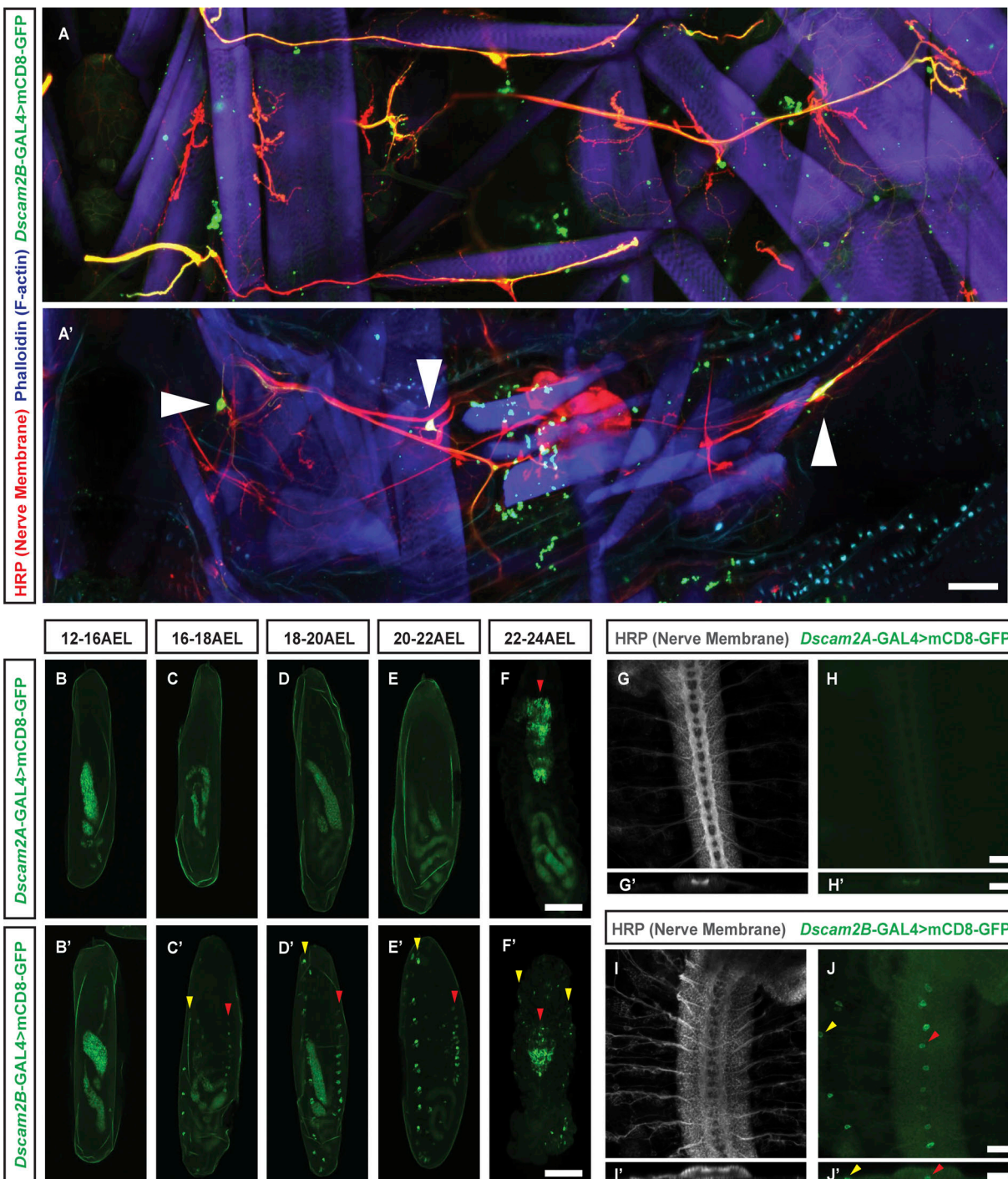


Figure S1. ***Dscam2* single isoform splice trap expression patterns in larvae and embryos.** (A and A') Co-labeling of HRP (red), phalloidin (blue), and *Dscam2B*>CD8GFP (green) in a single peripheral body-wall hemi-segment of a filleted third-instar larva. NMJs (red) and sensory neurons (white arrowheads) are seen in internal musculature (A) and external musculature (A'). Scale bar, 50 μm. (B-F') Representative images of *Dscam2A*>CD8GFP (B-F) and *Dscam2B*>CD8GFP (B'-F') expression pattern in embryos aged 12-24 h AEL. Red arrowheads indicate central nervous system neurons, and yellow arrowheads indicate PNS neurons. Scale bar, 100 μm. (G-J') Co-labeling of HRP (gray) and *Dscam2A*>CD8GFP (green, G-H') and *Dscam2B*>CD8GFP (green, I-J') of filleted stage 16 embryos. Arrowheads as in B-F'. Scale bars, 20 μm.

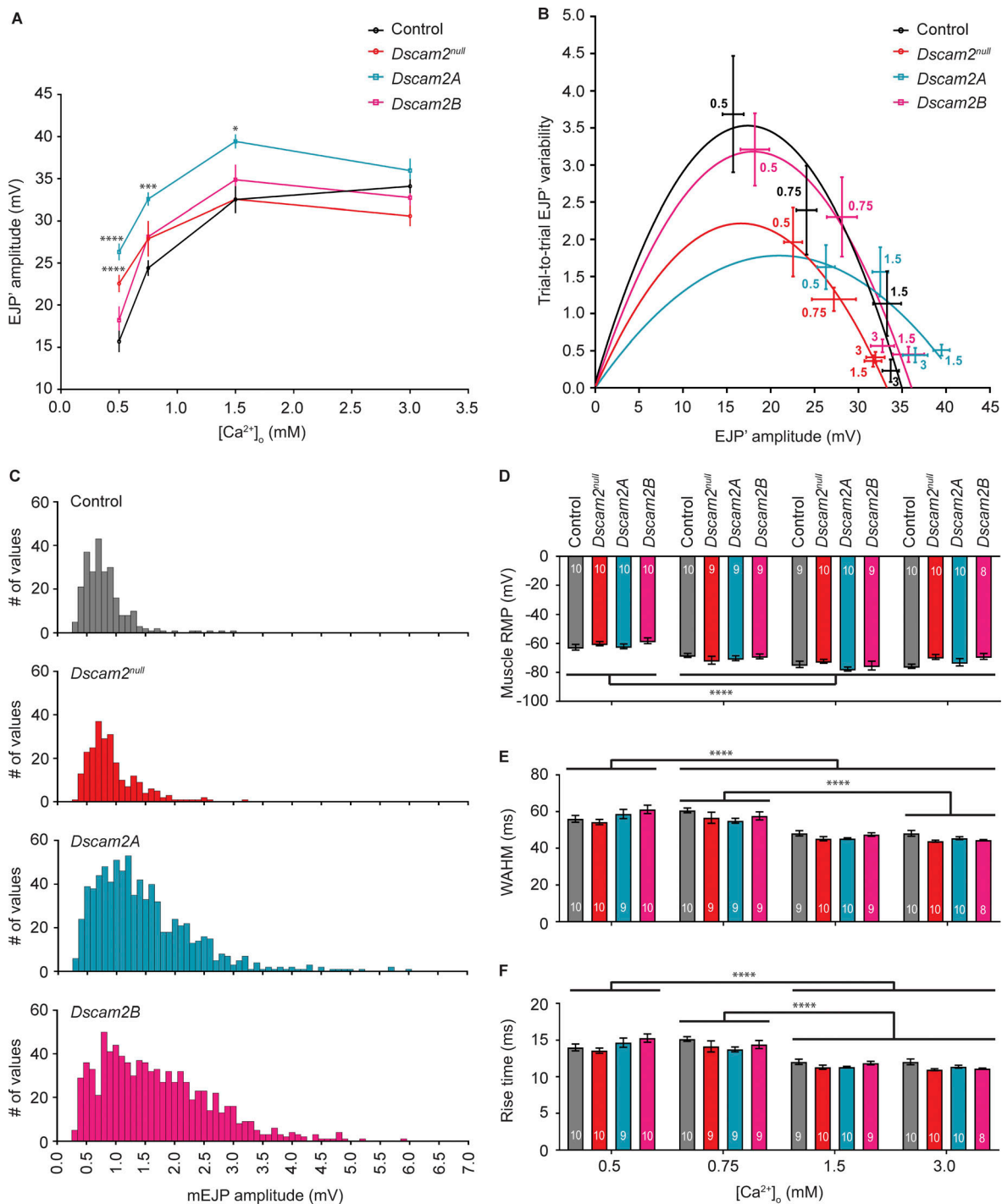


Figure S2. **Electrophysiological analyses of *Dscam2* mutant NMJs.** (A) Quantification of evoked junctional potentials corrected for nonlinear summation (EJP') in control (black), *Dscam2<sup>null</sup>* (red), *Dscam2A* (blue), and *Dscam2B* (magenta) at 0.5, 0.75, 1.5, and 3 mM of [Ca<sup>2+</sup>]<sub>o</sub>. *n* = 8–10. (B) Variance-amplitude plots of control (black), *Dscam2<sup>null</sup>* (red), *Dscam2A* (blue), and *Dscam2B* (magenta) with lines of best fit generated by nonlinear (quadratic) regression. Error bar crosses represent SEM for trial-to-trial EJP' variability (vertical error bars) and EJP' amplitude (horizontal error bars), with corresponding nearby numbers indicating [Ca<sup>2+</sup>]<sub>o</sub>. *n* = 7–10. (C) Representative frequency histograms for mEJP amplitude from individual NMJs. (D–F) Quantification of muscle resting membrane potential (RMP; D), EJP width at half maximum (WAHM; E), and EJP rise time (F). *n* indicated in graph. Data shown as mean ± SEM; two-way ANOVA; groups within conditions compared with Sidak's post-test. \*, *P* < 0.05; \*\*, *P* < 0.001; \*\*\*, *P* < 0.0001 for all panels.

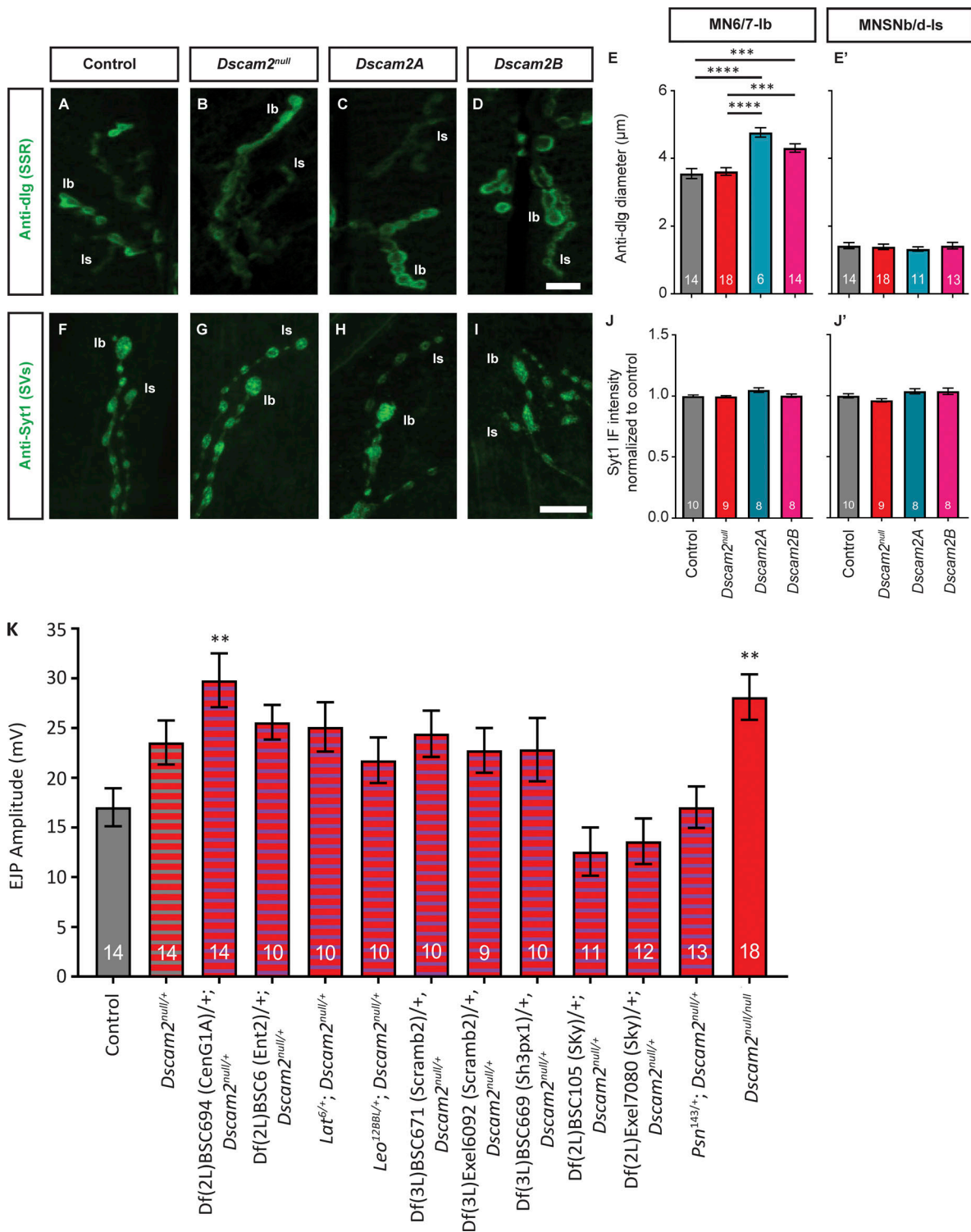


Figure S3. **Synaptic marker immunoreactivity at *Dscam2* mutant NMJs and results from the *Dscam2* interactor candidate screen.** (A–D) Representative images of dlg immunoreactivity in control (A), *Dscam2<sup>null</sup>* (B), *Dscam2A* (C), and *Dscam2B* (D) in MN6/7-Ib (Ib) and MNSNb/d-Ib (Is). Scale bar, 10 µm. (E and E') Quantification of diameter of anti-dlg immunoreactivity surrounding boutons. Data shown as mean ± SEM, n indicated in graph; one-way ANOVA; groups compared with Tukey's post-test. \*\*\*, P < 0.001; \*\*\*\*, P < 0.0001. (F–I) Representative images of anti-Syt1 immunoreactivity in control (F), *Dscam2<sup>null</sup>* (G), *Dscam2A* (H), and *Dscam2B* (I) in Ib and Is. Scale bar, 10 µm. (J and J') Quantification of anti-Syt1 immunofluorescence (IF) intensity relative to control. Data shown as mean ± SEM; n indicated in graph; one-way ANOVA; groups compared with Tukey's post-test. (K) Quantification of EJP amplitude in different combinations of genotypes. Stock numbers listed in Materials and Methods. Data shown as mean ± SEM; n indicated in graph. Kruskal-Wallis test; groups compared with Dunn's post-test. \*\*, P < 0.01. IF, immunofluorescence.

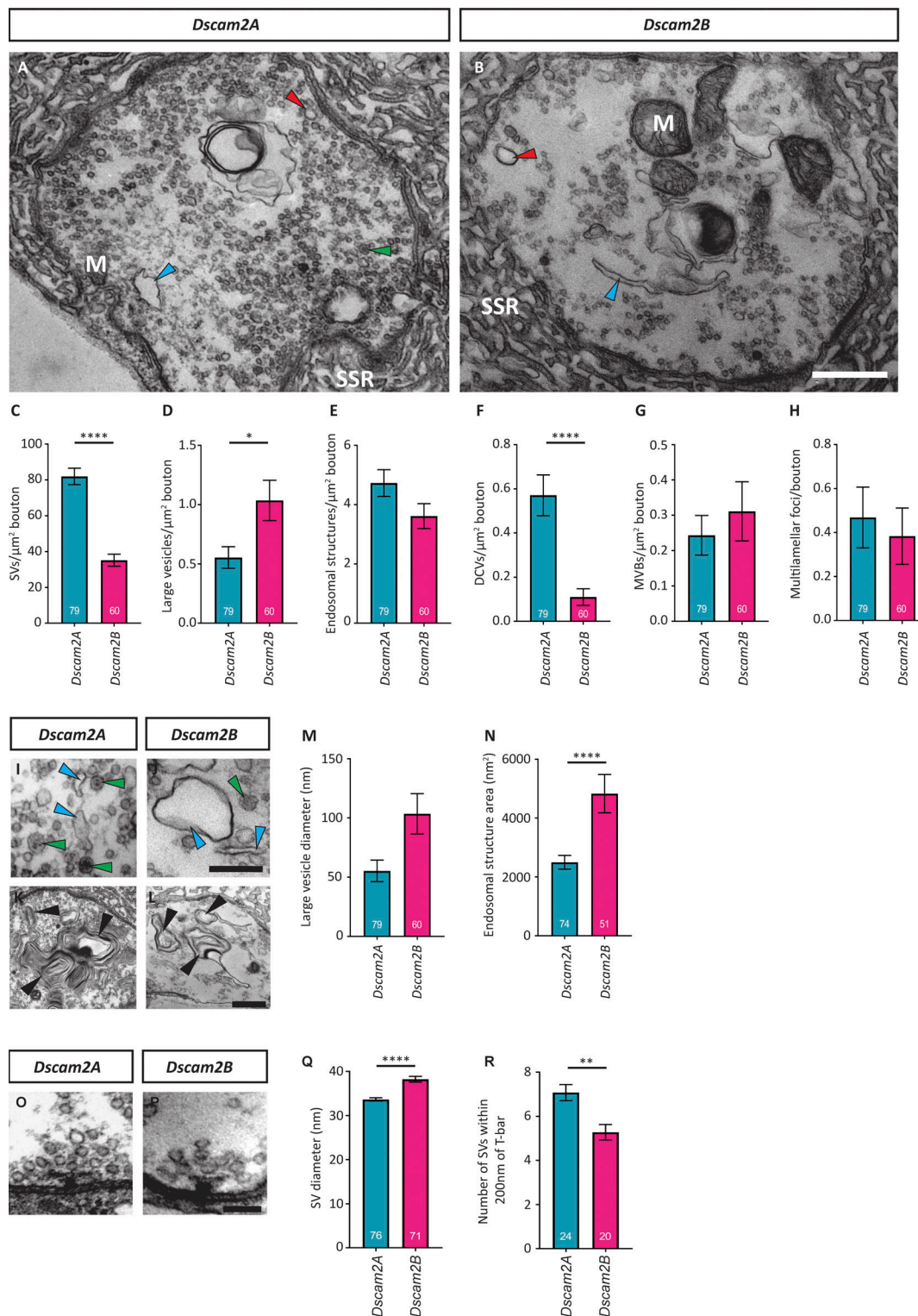


Figure S4. **Ultrastructural analyses of *Dscam2* single isoform mutant boutons reveal endosomal defects.** (A and B) Representative electron micrographs of *Dscam2A* (A) and *Dscam2B* (B) boutons. Arrowheads indicate examples of large vesicles (red), tubular endosomes (blue), and DCVs (green). Mitochondria (M) and SSR indicated in white text. Scale bar, 500 nm. (C–H) Quantification of synaptic vesicle (SV) density (C), large vesicle density (D), tubular endosome density (E), DCV density (F), MVB density (G), and density of multilamellar foci (H; Mann-Whitney rank-sum test). (I–L) Representative electron micrographs of DCVs (green arrowheads) and endosomes (blue arrowheads) in *Dscam2A* (I) and *Dscam2B* (J). Scale bar, 200 nm. Also shown are examples of multilamellar foci (black arrowheads) in *Dscam2A* (K) and *Dscam2B* (L). Scale bar, 100 nm. (M and N) Quantification of diameter of large vesicles (M) and cross-sectional area of endosomes (N; Mann-Whitney rank-sum test). (O and P) Representative electron micrographs of *Dscam2A* (O) and *Dscam2B* (P) T-bars. Scale bar, 100 nm. (Q and R) Quantification of SV diameter (Q) and number of SVs within 200 nm of T-bar (R; unpaired Student's *t* test). Data shown as mean  $\pm$  SEM; *n* indicated in graph. \*,  $P > 0.05$ ; \*\*,  $P < 0.01$ ; \*\*\*,  $P < 0.0001$  for all panels.

Provided online is one supplemental table. Table S1 shows known properties of all larval abdominal segment motor neurons including expression of *Dscam2B*.